Journal of Computational Physics 229 (2010) 4159–4182

Contents lists available at ScienceDirect

Journal of Computational Physics

journal homepage: www.elsevier.com/locate/jcp

Discretization correction of general integral PSE Operators for particle methods

Birte Schrader, Sylvain Reboux, Ivo F. Sbalzarini *

Institute of Theoretical Computer Science and Swiss Institute of Bioinformatics, ETH Zurich, Universitätsstr. 6, CH-8092 Zurich, Switzerland

ARTICLE INFO

Article history:
Received 25 March 2009
Received in revised form 14 December 2009
Accepted 5 February 2010
Available online 14 February 2010

Keywords:
Integral operator
Particle method
Kernel normalization
Error analysis
Particle strength exchange
Overlap condition

ABSTRACT

The general integral particle strength exchange (PSE) operators [J.D. Eldredge, A. Leonard, T. Colonius, J. Comput. Phys. 180 (2002) 686–709] approximate derivatives on scattered particle locations to any desired order of accuracy. Convergence is, however, limited to a certain range of resolutions. For high-resolution discretizations, the constant discretization error dominates and prevents further convergence. We discuss a consistent discretization correction framework for PSE operators that yields the desired rate of convergence for any resolution, both on uniform Cartesian and irregular particle distributions, as well as near boundaries. These discretization-corrected (DC) PSE operators also have no overlap condition, enabling the kernel width to become arbitrarily small for constant interparticle spacing. We show that, on uniform Cartesian particle distributions, this leads to a seamless transition between DC PSE operators and classical finite difference stencils. We further identify relationships between DC PSE operators and operators used in corrected smoothed particle hydrodynamics and reproducing kernel particle methods. We analyze the presented DC PSE operators with respect to accuracy, rate of convergence, computational efficiency, numerical dispersion, numerical diffusion, and stability.

1. Introduction

Lagrangian particle methods for the simulation of continuum systems, such as smoothed particle hydrodynamics (SPH) or vortex methods, rely on accurate and efficient evaluation of spatial derivatives of a function that is discretized over scattered particle locations. Eldredge et al. [1] presented a unified approach to approximate spatial derivatives of any degree. It is based on a generalization of the integral particle strength exchange (PSE) operators introduced by Degond and Mas-Gallic [2] to approximate the Laplacian in convection–diffusion problems. These integral operators are usually discretized by midpoint quadrature over the particle positions. The discretized integral operators thus involve two errors: the mollification error and the discretization error. In order for the discretized operator to be consistent, the interparticle spacing h and the width ε of the operator kernel (not to be confused with the mollification kernel used for function representation) have to satisfy the condition $c = h/\varepsilon \to 0$ as h and ε tend to zero [3,4]. This leads to an "overlap condition" of the type $h \leqslant a\varepsilon^q, 0 < a < 1, q > 1$, thus typically requiring large numbers of particles (increasing as ε^{-qn} in $\mathbb{R}^n$) for small kernel sizes.

This constraint can be relaxed by replacing the continuous moment conditions that are used to derive the operator kernel [1] by the corresponding discrete moment conditions. Using such discretization-corrected (DC) kernels ensures that the discretization error can not dominate the overall order of accuracy of the approximation. DC operators are always consistent, independent of the ratio $c = h/\varepsilon$, thus eliminating the need for the overlap condition $c < 1$ for the operator kernel, as well as for $c \to 0$ as $h, \varepsilon \to 0$.

* Corresponding author. Tel.: +41 44 632 6344; fax: +41 44 632 1562.
E-mail addresses: birte@ethz.ch (B. Schrader), sylvain.reboux@inf.ethz.ch (S. Reboux), ivos@ethz.ch (I.F. Sbalzarini).

0021-9991/$ - see front matter © 2010 Elsevier Inc. All rights reserved.
doi:10.1016/j.jcp.2010.02.004

To the best of our knowledge, discretization correction for particle methods was first described by Cottet et al. [5] for interpolation kernels. Since then, it has been used in many state-of-the-art simulations. Hieber and Koumoutsakos [6], for example, used it for a second-order approximation of the Laplacian on symmetric particle distributions. Bergdorf et al. [7] pointed out the possibility of discretization correction of the anisotropic diffusion operator derived by Degond and Mas-Gallic [8]. Sbalzarini et al. used DC PSE operators to approximate the Laplacian with second-order accuracy [9] on uniform Cartesian particle distributions. Poncet [10] used the original and the DC anisotropic diffusion operators in vortical ring simulations and compared the results to classical finite difference (FD) stencils. His corrected operator is of order one on arbitrary particle distributions and of order two on symmetric ones. Golia et al. [11] formulated two different discretization corrections for PSE operators to estimate the gradient and the Laplacian of a field. Their corrected operators guarantee second-order accuracy on symmetric particle distributions and first- or zeroth-order on arbitrary particle distributions. In all these previous applications of DC PSE operators, however, little attention has been paid to their numerical properties, and no general analysis has been published so far. The use of DC PSE operators on moving particles is computationally expensive since a linear system of equations has to be solved for each particle whenever particles have moved. In order to maintain the order of accuracy, while keeping the computational cost low, the particles can be reinitialized on a Cartesian grid ("remeshed") at each time step (see for example Bergdorf et al. [7]) or every few time steps (see for example Koumoutsakos [12]). Other authors combined diffusion and remeshing into a single kernel [13] to further reduce the computational cost.

In the present paper, we present a formal framework for DC PSE operators, and we derive expressions for their overall approximation errors. We also show the relationships between DC PSE operators, FD stencils, and the operators used in corrected SPH [14–20] and reproducing kernel particle methods (RKPM) [21,22]. We perform a full stability analysis based on the dispersive and diffusive properties of the operators and show the convergence rates and computational efficiencies of the operators on several test problems. In all cases, we compare the DC PSE operators to the original (uncorrected) ones. Our analysis considers particles distributed both irregularly and on a uniform Cartesian grid. In addition, we also discuss and assess boundary effects. The influences of the free operator parameters (ratio $c = h/\varepsilon$, cutoff radius r_c, and order of accuracy r) on the computational efficiency and the operators' numerical properties are discussed in all cases.

The paper is organized as follows: in the following section, we present a formal DC framework for the general integral PSE operators introduced by Eldredge et al. [1]. This provides the theoretical background for Section 3, where we outline the relationships between DC PSE operators, FD stencils, and other operators used in particle methods. We show that DC PSE operators in some cases become algebraically equivalent to FD stencils in the limit of infinitely small kernel widths. In Section 4, we numerically compare the convergence rates and the computational efficiencies of uncorrected and corrected PSE operators and the limiting FD stencils on uniform Cartesian particle distributions, arbitrary particle distributions, and near boundaries. In Section 5, we quantify the numerical dispersion and diffusion introduced by the corrected and uncorrected operators. Closed-form stability conditions are given for uniform and non-uniform particle distributions based on the modified wavenumbers. Our conclusions and open questions are summarized in Section 6.

2. Discretization correction of general integral PSE operators

PSE operators approximate any spatial derivative

$$D^{\boldsymbol{\beta}} f(\boldsymbol{x}) = \frac{\partial^{|\boldsymbol{\beta}|} f(\boldsymbol{x})}{\partial x_1^{\beta_1} \partial x_2^{\beta_2} \dots \partial x_n^{\beta_n}} \tag{1}$$

of a (sufficiently smooth) field f by an integral operator over scattered particle locations [1]:

$$Q^{\boldsymbol{\beta}} f(\boldsymbol{x}) = \frac{1}{\varepsilon^{|\boldsymbol{\beta}|}} \int_{\mathbb{R}^n} (f(\boldsymbol{y}) \pm f(\boldsymbol{x})) \eta_\varepsilon^{\boldsymbol{\beta}}(\boldsymbol{x} - \boldsymbol{y}) d\boldsymbol{y} = D^{\boldsymbol{\beta}} f(\boldsymbol{x}) + \mathcal{O}(\varepsilon^r). \tag{2}$$

The operator kernel $\eta_\varepsilon^{\boldsymbol{\beta}}(\boldsymbol{z}) = \varepsilon^{-n} \eta^{\boldsymbol{\beta}}(\boldsymbol{z}/\varepsilon)$ is scaled to width ε (kernel width) and chosen such as to fulfill continuous moment conditions [1]. The sign in Eq. (2) is chosen positive for odd $|\boldsymbol{\beta}|$ and negative for even $|\boldsymbol{\beta}|$. This convention will be used throughout the paper. The modulus of the multiindex $\boldsymbol{\beta}, \boldsymbol{\beta} \in \mathbb{N}^n$, is defined as $|\boldsymbol{\beta}| = \sum_{i=1}^n \beta_i$. Moreover, $\boldsymbol{x}^{\boldsymbol{\beta}} = \prod_{i=1}^n x_i^{\beta_i}$ and $\boldsymbol{\beta}! = \prod_{i=1}^n \beta_i!$. A sum over all indices $\boldsymbol{\beta}$ for which $|\boldsymbol{\beta}| = k$ is written as $\sum_{|\boldsymbol{\beta}|=k}$. Here and in the sequel, n is the number of space dimensions and $\boldsymbol{e}_i$ the unit vector along dimension i.

The integral operator in Eq. (2) is discretized by midpoint quadrature over the particles, thus,

$$Q_h^{\boldsymbol{\beta}} f(\boldsymbol{x}) = \frac{1}{\varepsilon^{|\boldsymbol{\beta}|}} \sum_{p \in \mathcal{N}(\boldsymbol{x})} v_p (f(\boldsymbol{x}_p) \pm f(\boldsymbol{x})) \eta_\varepsilon^{\boldsymbol{\beta}}(\boldsymbol{x} - \boldsymbol{x}_p), \tag{3}$$

where $\boldsymbol{x}_p$ and v_p are the position and the volume of particle p, respectively, and $\mathcal{N}(\boldsymbol{x})$ is the set of all particles in an r_c-neighborhood around $\boldsymbol{x}$. The cutoff radius r_c of the operator is defined such that $\mathcal{N}(\boldsymbol{0})$ approximates the support of $\eta_\varepsilon^{\boldsymbol{\beta}}$ with a certain accuracy. The resolution of the discretization is given by the characteristic interparticle spacing h, defined as the nth root of the average particle volume.

Using Eq. (3) to compute Eq. (1) involves two approximations: the mollification error $Q^{\boldsymbol{\beta}} f(\boldsymbol{x}) - D^{\boldsymbol{\beta}} f(\boldsymbol{x})$ and the discretization error $Q_h^{\boldsymbol{\beta}} f(\boldsymbol{x}) - Q^{\boldsymbol{\beta}} f(\boldsymbol{x})$. While these two error terms are usually treated separately in particle methods, we directly

consider the overall error $\epsilon(\boldsymbol{x}) = Q_h^{\beta} f(\boldsymbol{x}) - D^{\beta} f(\boldsymbol{x})$. An expression for this error can be derived by expanding the field f in Eq. (3) into a Taylor series around $\boldsymbol{x}$ and subtracting $D^{\beta} f(\boldsymbol{x})$:

$$\epsilon(\boldsymbol{x}) = \left(\frac{(-1)^{|\beta|}}{\beta!} Z_h^{\beta}(\boldsymbol{x}) - 1 \right) D^{\beta} f(\boldsymbol{x}) + \sum_{\substack{|\alpha|=1 \\ \alpha \neq \beta}}^{\infty} \frac{(-1)^{|\alpha|}}{\alpha!} \varepsilon^{|\alpha|-|\beta|} Z_h^{\alpha}(\boldsymbol{x}) D^{\alpha} f(\boldsymbol{x}) + \epsilon_0, \tag{4}$$

with

$$\epsilon_0 = \begin{cases} 2\varepsilon^{-|\beta|} Z_h^{\mathbf{0}}(\boldsymbol{x}) f(\boldsymbol{x}), & |\beta| \text{ odd}, \\ 0, & |\beta| \text{ even}, \end{cases} \tag{5}$$

and the discrete moments Z_h^{α} defined as

$$Z_h^{\alpha}(\boldsymbol{x}) = \frac{1}{\varepsilon^n} \sum_{p \in \mathcal{N}(\boldsymbol{x})} v_p \left(\frac{\boldsymbol{x} - \boldsymbol{x}_p}{\varepsilon} \right)^{\alpha} \eta^{\beta} \left(\frac{\boldsymbol{x} - \boldsymbol{x}_p}{\varepsilon} \right). \tag{6}$$

Directly considering the overall error in Eq. (4) enables deriving a consistent discretization framework by modifying the kernel function η^{β} such that all error terms of order $s < r$ vanish. This can be accomplished by requiring the discrete moments Z_h^{β} to satisfy the conditions

$$Z_h^{\alpha} \begin{cases} = (-1)^{|\beta|} \beta!, & \alpha = \beta, \\ = 0, & \alpha \neq \beta, \quad \alpha_{\min} \leqslant |\alpha| \leqslant |\beta| + r - 1, \quad \alpha_{\min} = \begin{cases} 0, & |\beta| \text{ odd}, \\ 1, & |\beta| \text{ even}, \end{cases} \\ < \infty, & |\alpha| = |\beta| + r. \end{cases} \tag{7}$$

These discrete conditions are analogous to the continuous ones [1]. Satisfying the continuous moment conditions, however, may not be sufficient for convergence of the overall error when keeping the ratio c constant. The uncorrected kernel η^{β} fulfills the discrete moment conditions only in the limit $c \to 0$, where the discrepancy between the discrete moments (Eq. (6)) and the continuous ones ($\sum_{p \in \mathcal{N}(\boldsymbol{x})} v_p$ in Eq. (6) replaced by $\int_{\mathbb{R}^n} d\boldsymbol{x}$) vanishes. Depending on the desired accuracy, uncorrected kernels may still be satisfactory for small enough c. Error terms proportional to ε^s with $s < r$ do, however, exist and can become dominant for high resolutions when $c = h/\varepsilon$ is kept constant. Discretization correction aims at removing those error terms by designing kernels that directly fulfill the discrete moment conditions in Eq. (7). This can be done by including a correction function $C(\boldsymbol{z}, \boldsymbol{x})$ into the kernel, where $\boldsymbol{x}$ is the position where the operator is evaluated and $\boldsymbol{z}$ is a location in a local coordinate system with origin at $\boldsymbol{x}$.

We restrict the number of possible DC PSE kernels by constructing them according to the following template:

$$\eta^{\beta}(\boldsymbol{z}, \boldsymbol{x}) = \left(\sum_{|\gamma|=\alpha_{\min}}^{|\beta|+r-1} a_{\gamma}(\boldsymbol{x}) \boldsymbol{z}^{\gamma} \right) e^{-|\boldsymbol{z}|^2} = C(\boldsymbol{z}, \boldsymbol{x}) e^{-|\boldsymbol{z}|^2}, \tag{8}$$

with a polynomial correction function $C(\boldsymbol{z}, \boldsymbol{x})$. We choose this template due to its simplicity and similarity to the kernel functions proposed for the original PSE operators [1]. Kernels with a small number of sign changes generally have better accuracy and robustness [23,24]. Moreover, the non-vanishing discrete moments Z_h^{α}, $|\alpha| = |\beta| + r$, should be as small as possible in order to minimize the leading error term.

The unknown coefficients $a_{\gamma}(\boldsymbol{x})$ in Eq. (8) are determined by solving a linear system of equations. This is obtained by substituting the discrete moments of the kernel template (Eq. (8)) into the conditions in Eq. (7):

$$\sum_{|\gamma|=\alpha_{\min}}^{|\beta|+r-1} a_{\gamma}(\boldsymbol{x}) w_{\alpha\gamma}(\boldsymbol{x}) = \begin{cases} (-1)^{|\beta|} \beta!, & \alpha = \beta, \\ 0, & |\alpha| \neq |\beta|, \end{cases} \qquad \forall \alpha, \ \alpha_{\min} \leqslant \alpha \leqslant |\beta| + r - 1, \tag{9}$$

with weights

$$w_{\alpha,\gamma}(\boldsymbol{x}) = \frac{1}{\varepsilon^{|\alpha+\gamma|+n}} \sum_{p \in \mathcal{N}(\boldsymbol{x})} v_p (\boldsymbol{x} - \boldsymbol{x}_p)^{\alpha+\gamma} e^{-\left|\frac{\boldsymbol{x}-\boldsymbol{x}_p}{\varepsilon}\right|^2}. \tag{10}$$

This linear system consists of m equations for m unknowns, where

$$m = \binom{|\beta| + r - 1 + n}{n} - \alpha_{\min}. \tag{11}$$

The multiindices α identify the equations (rows), and the multiindices γ identify the unknown coefficients (columns). While the continuous moment conditions are often redundant [1], this is not the case for the discrete ones, and the full set of m equations must generally be considered. The condition number of this linear system is determined by the particle distribution and the choice of kernel function template [25].

For uniform particle distributions, the coefficients a_γ are independent of $\boldsymbol{x}_p$. The linear system (Eq. (9)) thus needs to be solved only once, and the same kernel can be used at all particle positions. Moreover, for symmetric particle distributions all odd moments of even function terms and even moments of odd function terms vanish. All coefficients a_γ for which $\boldsymbol{\gamma}+\boldsymbol{\beta}$ contains odd elements can therefore be set to zero *a priori*. The system of equations can thus be reduced to size

$$m_{\text{symm}} = \binom{\left\lfloor \frac{|\boldsymbol{\beta}|+r-1}{2} \right\rfloor + n}{n} - \alpha_{\min}$$

by removing all rows and columns where $\boldsymbol{\alpha}+\boldsymbol{\beta}$ or $\boldsymbol{\gamma}+\boldsymbol{\beta}$ contain odd elements.

For non-uniform particle distributions, the weights in Eq. (10) are functions of $\boldsymbol{x}$. In this case, a different linear system has to be solved at every particle position $\boldsymbol{x}_p$. The coefficients $a_\gamma(\boldsymbol{x})$ of the DC PSE kernels may thus be different on different particles and have to be recomputed whenever particles have moved. For small m (low-order kernels for derivatives of small degree in low-dimensional spaces), this can efficiently be done using a closed-form expression for the coefficients $a_\gamma(\boldsymbol{x})$ as a function of the weights $w_{\gamma,\boldsymbol{\alpha}}(\boldsymbol{x})$. In addition, the matrix of weights is symmetric if the moment conditions are properly ordered, and it typically contains several identical entries since $w_{\boldsymbol{i},\boldsymbol{j}}(\boldsymbol{x}) = w_{\boldsymbol{k},\boldsymbol{l}}(\boldsymbol{x}) \forall \boldsymbol{x}$ if $\boldsymbol{i}+\boldsymbol{j}=\boldsymbol{k}+\boldsymbol{l}$.

Since the DC operators on non-uniformly distributed particles depend on particle position, particle–particle interactions are not necessarily symmetric any more. This increases the computational cost of a simulation by up to a factor of two and impairs the exact conservativeness of the uncorrected full-space PSE operators [17]. For first-order accurate operators, this can be remedied by using different correction functions for each pair of particles [18–20]. These correction functions are averages of the kernel correction functions at the two particle positions. Preserving symmetry for higher-order DC PSE operators is, to our knowledge, an open problem.

3. Related operators

For certain parameter choices, DC PSE operators become equivalent or similar to operators used in other numerical methods. We particularly highlight the connections with FD stencils, corrected SPH, and operators used in RKPM. In fact, we prove that certain classical FD stencils are limit cases of DC PSE operators for $c \to \infty$.

3.1. FD stencils

For uniform Cartesian particle distributions with spacing h and a finite operator support of radius r_c, the discrete integral operator (Eq. (3)) can be rewritten as

$$Q_h^{\boldsymbol{\beta}} f(\boldsymbol{x}) = \frac{c^n}{\mathcal{E}^{|\boldsymbol{\beta}|}} \sum_{|\boldsymbol{k}|^2=0}^{\lfloor r_c^2/h^2 \rfloor} (f(\boldsymbol{x}+\boldsymbol{k}h) \pm f(\boldsymbol{x})) \eta^{\boldsymbol{\beta}}(-c\boldsymbol{k}), \quad \boldsymbol{k} \in \mathbb{Z}^n. \tag{12}$$

Using the kernel template given in Eq. (8), the value of the DC kernel function at $-c\boldsymbol{k}$ is

$$\eta^{\boldsymbol{\beta}}(-c\boldsymbol{k}) = \left(\sum_{\substack{|\boldsymbol{\gamma}|=\alpha_{\min} \\ \boldsymbol{\beta}+\boldsymbol{\gamma} \text{ even}}}^{|\boldsymbol{\beta}|+r-1} a_\gamma (-c\boldsymbol{k})^\gamma \right) e^{-c^2|\boldsymbol{k}|^2}, \tag{13}$$

and the discrete moments become

$$Z_h^{\boldsymbol{\alpha}} = c^n \sum_{|\boldsymbol{k}|^2=0}^{\lfloor r_c^2/h^2 \rfloor} \sum_{\substack{|\boldsymbol{\gamma}|=\alpha_{\min} \\ \boldsymbol{\beta}+\boldsymbol{\gamma} \text{ even}}}^{|\boldsymbol{\beta}|+r-1} a_\gamma (c\boldsymbol{k})^{\boldsymbol{\alpha}+\boldsymbol{\gamma}} e^{-c^2|\boldsymbol{k}|^2}. \tag{14}$$

Here, "$\boldsymbol{\beta}+\boldsymbol{\gamma}$ even" stands for all multiindices $\boldsymbol{\gamma}$ for which $\boldsymbol{\beta}+\boldsymbol{\gamma}$ contains only even elements. All other $\boldsymbol{\gamma}$ need not be considered since the corresponding coefficients a_γ can *a priori* be set to zero (see Section 2).

The DC PSE operators for $c \to \infty$ can be derived from Eqs. (12)–(14) and the moment conditions (Eq. (7)). For the second-order accurate DC PSE operator approximating the first derivative along dimension i ($r=2, \boldsymbol{\beta}=\boldsymbol{e}_i$), for example, the DC kernel function can be written as

$$\eta^{\boldsymbol{e}_i}(-c\boldsymbol{k}) = \frac{k_i e^{-c^2|\boldsymbol{k}|^2}}{c^{n+1} \sum_{|\boldsymbol{l}|^2=0}^{\lfloor r_c^2/h^2 \rfloor} l_i^2 e^{-c^2|\boldsymbol{l}|^2}}. \tag{15}$$

Using this kernel, the operator (Eq. (12)) becomes

$$Q_h^{\boldsymbol{e}_i} f(\boldsymbol{x}) = \frac{\sum_{|\boldsymbol{k}|^2=0}^{\lfloor r_c^2/h^2 \rfloor} (f(\boldsymbol{x}+\boldsymbol{k}h) + f(\boldsymbol{x})) k_i e^{-c^2|\boldsymbol{k}|^2}}{h \sum_{|\boldsymbol{k}|^2=0}^{\lfloor r_c^2/h^2 \rfloor} k_i^2 e^{-c^2|\boldsymbol{k}|^2}}.$$

This is a FD stencil with extent and weights that can be adjusted by the choice of the cutoff radius r_c and the ratio c. Letting $c \to \infty$ yields

$$\lim_{c\to\infty} Q_h^{\boldsymbol{e}_i} f(\boldsymbol{x}) = \frac{f(\boldsymbol{x}+\boldsymbol{h}_i) - f(\boldsymbol{x}-\boldsymbol{h}_i)}{2h}, \quad \boldsymbol{h}_i = h\boldsymbol{e}_i, \tag{16}$$

for any value of $r_c \geqslant h$. This is the classical centered difference stencil for the first derivative of f.

Following the same procedure, the second-order DC PSE operator approximating the Laplacian $\Delta f(\boldsymbol{x}) = \nabla^2 f(\boldsymbol{x})$ becomes

$$\lim_{c\to\infty} Q_h^{\mathrm{Lap}} f(\boldsymbol{x}) = \lim_{c\to\infty} \sum_{i=1}^{n} Q_h^{2\boldsymbol{e}_i} f(\boldsymbol{x}) = \frac{\sum_{i=1}^{n} [f(\boldsymbol{x}+\boldsymbol{h}_i) - 2f(\boldsymbol{x}) + f(\boldsymbol{x}-\boldsymbol{h}_i)]}{h^2}, \tag{17}$$

and the fourth-order DC PSE approximation of the first derivative along $\boldsymbol{e}_i$ yields

$$\lim_{c\to\infty} Q_h^{\boldsymbol{e}_i} f(\boldsymbol{x}) = \frac{-f(\boldsymbol{x}+2\boldsymbol{h}_i) + 8f(\boldsymbol{x}+\boldsymbol{h}_i) - 8f(\boldsymbol{x}-\boldsymbol{h}_i) + f(\boldsymbol{x}-2\boldsymbol{h}_i)}{12h}. \tag{18}$$

The limit FD stencil of the n-dimensional anisotropic diffusion operator of order $r = 2$, introduced by Degond and Mas-Gallic [2] to approximate $\nabla \cdot (\boldsymbol{L}(\boldsymbol{x})\nabla f(\boldsymbol{x}))$, can be found in Appendix A. On Cartesian particle distributions, all these classical compact FD stencils can hence be interpreted as DC PSE operators with a kernel width ε tending to zero (grid points).

For irregular particle distributions, the DC PSE operators can be made equivalent to FD stencils for irregular meshes. Demkowicz et al. [26] proposed simple FD stencils approximating the two-dimensional Laplacian on irregular meshes by solving a linear system of equations consisting of moment conditions analogous to the ones used here for DC PSE operators. The value $\eta^{\beta}(\boldsymbol{x}-\boldsymbol{x}_p, \boldsymbol{x})$ of the DC PSE kernel is equivalent to the FD stencil weight α_p for particle (mesh node) p.

Wright and Fornberg [27] used radial basis functions to generate compact FD stencils on irregularly distributed nodes. For Cartesian node distributions, they recover the classical one- and two-dimensional FD stencils for first and second derivatives. These stencils were obtained in the limit of the radial basis function becoming flat, thus $c \to 0$. This was possible because the support of the stencils was chosen and fixed *a priori*. The DC PSE operator in Eq. (12) becomes equal to the respective FD stencil (Eqs. (16)–(18)) if one fixes r_c to the radius of the stencil. The limit $c \to \infty$ in our case, however, makes it unnecessary to fix r_c beforehand. Instead, compact FD stencils naturally emerge.

3.2. Normalized smoothing functions in (corrected) SPH

In PSE operators, the kernel is weighted by a sum or difference of field values, which guarantees conservativeness of DC PSE operators on uniform particle distributions. The operators used in SPH lack this symmetry. Rather, the kernel is weighted only by the field values evaluated at the particle locations:

$$Q_{h,\mathrm{SPH}}^{\beta} f(\boldsymbol{x}) = \frac{1}{\varepsilon^{|\beta|}} \sum_{p\in\mathcal{N}(\boldsymbol{x})} v_p f(\boldsymbol{x}_p) \eta_{\varepsilon,\mathrm{SPH}}^{\beta}(\boldsymbol{x}-\boldsymbol{x}_p). \tag{19}$$

This operator achieves rth-order convergence for all kernels $\eta_{\varepsilon,\mathrm{SPH}}^{\beta}$ that satisfy the discrete moment conditions

$$Z_h^{\alpha}(\boldsymbol{x}) = \frac{1}{\varepsilon^{|\alpha|+n}} \sum_{p\in\mathcal{N}(\boldsymbol{x})} v_p (\boldsymbol{x}_p - \boldsymbol{x})^{\alpha} \eta_{\varepsilon,\mathrm{SPH}}^{\beta}(\boldsymbol{x}-\boldsymbol{x}_p) \begin{cases} = \beta!, & \alpha = \beta, \\ = 0, & \alpha \neq \beta, \quad 0 \leqslant |\alpha| \leqslant |\beta| + r - 1, \\ < \infty, & |\alpha| = |\beta| + r. \end{cases} \tag{20}$$

In classical SPH, however, the kernel is designed to satisfy continuous moment conditions, and the above ones are not automatically fulfilled.

Johnson and Beissel [14] therefore introduced normalized smoothing functions for SPH. Hereby, $\eta_{\varepsilon,\mathrm{SPH}}^{\beta}$ is normalized with a scalar factor that depends on $\boldsymbol{x}$ such that the first condition in Eq. (20) is met. This is reminiscent of the corrected kernel function in Eq. (15), where the normalization factor is equal to the discrete moment $Z_h^{\boldsymbol{e}_i}$. Normalized SPH kernels were shown to lead to more accurate derivative estimations than unnormalized ones, especially near boundaries and on non-uniformly distributed particles [14]. Randles and Libersky [15] have extended the normalization idea to the estimation of the divergence of general tensor fields.

Bonet and Kulasegaram [16] derived second-order accurate SPH kernels for approximating a field, and first-order accurate kernels for approximating its Laplacian. These operators involve a linear correction function for the kernel, similar to the polynomial correction function proposed above. The coefficients of the correction function are chosen such as to satisfy the conditions in Eq. (20) for $|\alpha| \leqslant |\beta|$, hence $r = 1$ [16].

Lanson and Vila [18–20] proposed an altered normalization that leads to a conservative scheme for approximating first derivatives. This correction involves the PSE-like idea of replacing $f(\boldsymbol{x}_p)$ in Eq. (19) by the difference $f(\boldsymbol{x}_p) - f(\boldsymbol{x})$, such that the condition for $Z_h^{\boldsymbol{0}}$ vanishes. The average of the renormalization matrices at $\boldsymbol{x}$ and $\boldsymbol{x}_p$ is used as an additional weight. The resulting operators are first-order accurate and resemble DC PSE operators for even $|\beta|$. There is, however, no trivial conservative generalization of these operators to higher derivatives or higher orders of accuracy.

3.3. Reproducing kernel particle methods (RKPM)

In RKPM [21,22], a field $f(\boldsymbol{x})$ is represented using the particle function approximation

$$Q^{\mathbf{0}}_{h,\mathrm{RKPM}} f(\boldsymbol{x}) = \sum_{p \in \mathcal{N}(\boldsymbol{x})} v_p f(\boldsymbol{x}_p) \eta_{\varepsilon,\mathrm{RKPM}}(\boldsymbol{x} - \boldsymbol{x}_p, \boldsymbol{x}). \tag{21}$$

The order of accuracy is given by the largest integer r for which the interpolation kernel $\eta_{\varepsilon,\mathrm{RKPM}}$ fulfills the moment conditions

$$Z^{\mathbf{0}}_h(\boldsymbol{x}) = \frac{1}{\varepsilon^n} \sum_{p \in \mathcal{N}(\boldsymbol{x})} v_p \eta_{\varepsilon,\mathrm{RKPM}}(\boldsymbol{x} - \boldsymbol{x}_p, \boldsymbol{x}) = 1,$$

$$Z^{\boldsymbol{\alpha}}_h(\boldsymbol{x}) = \frac{1}{\varepsilon^{|\boldsymbol{\alpha}|+n}} \sum_{p \in \mathcal{N}(\boldsymbol{x})} v_p (\boldsymbol{x}_p - \boldsymbol{x})^{\boldsymbol{\alpha}} \eta_{\varepsilon,\mathrm{RKPM}}(\boldsymbol{x} - \boldsymbol{x}_p, \boldsymbol{x}) = 0, 1 \leqslant |\boldsymbol{\alpha}| \leqslant r - 1.$$

This is achieved by multiplying a window function by a polynomial correction function, thus forming the kernel η_{RKPM} similarly to Eq. (8). The $\boldsymbol{\beta}^{\mathrm{th}}$ derivative of the field is evaluated with an order of accuracy of $r - |\boldsymbol{\beta}|$ by taking the $\boldsymbol{\beta}^{\mathrm{th}}$ derivative of the continuously differentiable function approximation in Eq. (21). Just as corrected SPH operators, RKPM operators are not symmetric, making them generally non-conservative. When setting all particle volumes to $v_p \equiv 1$, RKPM become equivalent to moving least squares (MLS) approximations [28,29]. In MLS, non-uniform particle distributions (holes and clusters) are thus implicitly accounted for in the kernel function (shape function).

4. Convergence and computational efficiency of DC PSE operators

We present numerical experiments that illustrate the rate of convergence, overall error, and computational efficiency of DC PSE operators. We compare DC PSE operators to uncorrected PSE operators and to classical FD stencils. This section comprises four parts: In Section 4.1, convergence and computational efficiency are tested on uniform Cartesian particle distributions. The test problems are taken from Eldredge et al. [1] in order to demonstrate the fundamental characteristics of the operators. In Section 4.2, convergence is tested on irregular particle distributions and in Section 4.3, we assess boundary effects on finite-sized domains. Section 4.4 presents the operator's efficiency in practical applications by studying a two-dimensional Lagrangian advection–diffusion benchmark.

4.1. Uniform cartesian particle distributions

We present numerical experiments that demonstrate the rate of convergence and computational efficiency of DC PSE operators on uniform Cartesian particle distributions, and we compare the DC PSE operators to the corresponding limit FD stencils.

4.1.1. Rate of convergence

We consider the test case of evaluating the second derivative of the one-dimensional function

$$f(x) = \frac{1}{\sqrt{\pi\sigma^2}} e^{-x^2/\sigma^2}, \quad \sigma = 0.05, \tag{22}$$

at the locations of all particles in the domain $[-0.5, 0.5]$. The particles are arranged with equidistant spacing h and the ratio $c = h/\varepsilon$ is kept constant when the resolution is increased. We use the kernel function template

$$\eta^{\beta}(z) = z^{(\beta \bmod 2)} \left(\sum_{\gamma=0}^{m_{\mathrm{symm}}-1} a_\gamma |z|^\gamma \right) e^{-|z|^2}, \tag{23}$$

which typically yields higher accuracy for one-dimensional operators on symmetric particle distributions than the more general template of Eq. (8).

Fig. 1 shows the L_2 norm of the relative error[1] in the approximation of the derivative by Eq. (3) for different c and orders $r = 2$ (top row) and $r = 4$ (bottom row). The cutoff radii are $r_c = 3.5\varepsilon$ $(r = 2)$ and $r_c = 5.5\varepsilon$ $(r = 4)$ for the uncorrected operators, and $r_c = 2\varepsilon$ $(r = 2)$ and $r_c = 3\varepsilon$ $(r = 4)$ for the DC operators. The error of order $s = -2$ for very high resolutions is due to limited machine precision and numerical extinction. It is not a feature of the operators.

The uncorrected operators yield the desired rate of convergence over a wide range of resolutions if ratio c is small (e.g. $c = 0.5$, which is the ratio used by Eldredge et al.). For larger values of c (curves for $c = 0.9, c = 1.0$, and $c = 1.4$), the error reaches a constant plateau at lower resolutions. This is due to the constant discretization error of the quadrature. For small c, the density of quadrature points is higher and hence the discrete moment conditions are closer to the continuous ones. The constant minimum error level $E_{\min}$ for the uncorrected operators is given by the error term in Eq. (4) containing the discrete

[1] We normalize the error with the L_∞ norm of the exact solution in the domain of interest. We do not show the L_∞ norm of the relative errors since it shows the same behavior as the L_2 norm.

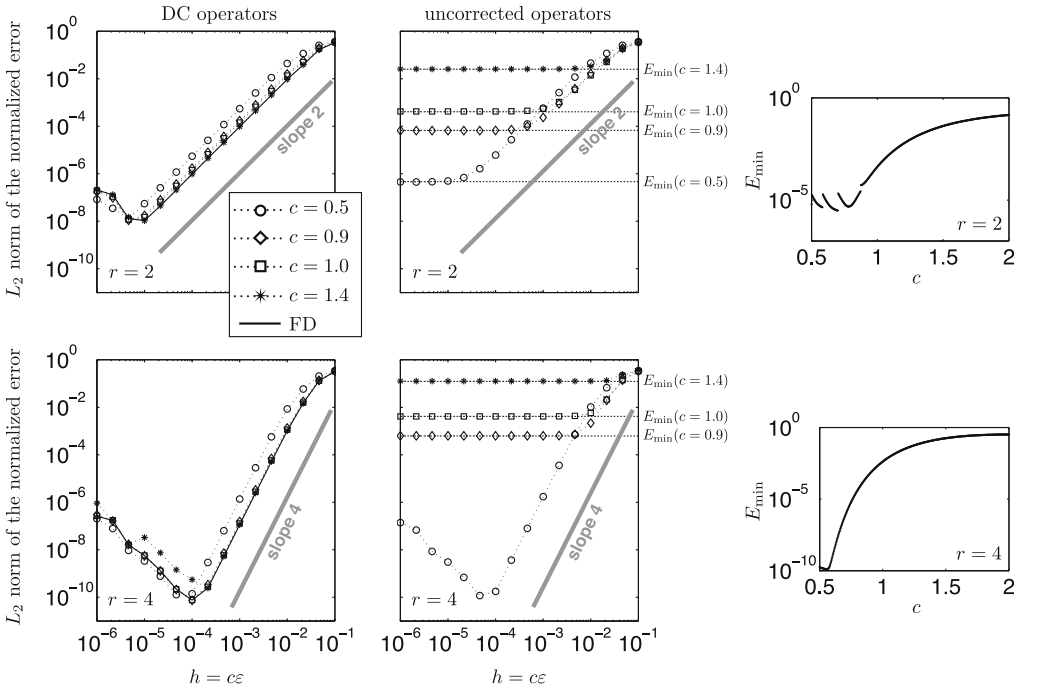

Fig. 1. Convergence of the DC PSE operator approximating the second derivative of Eq. (22) on uniform Cartesian particle distributions. We show the convergence of the relative error for DC (left) and uncorrected (center) PSE operators of orders $r = 2$ (top) and $r = 4$ (bottom). The panels on the right show the dependence of the minimum error level $E_{\min}$ of the uncorrected operators on the ratio $c = h/\varepsilon$.

moment Z_h^2. This moment increases with increasing c, as shown in the right-most panels of Fig. 1. The minimum error level decreases exponentially with c. This is due to the discretization error decreasing exponentially for an integrand following the template of Eq. (8) or (23) [30]. The discontinuities in $E_{\min}$ for small c and $r = 2$ are a result of the cutoff radius being fixed in terms of the kernel width ε: At the discontinuities, the number of particles in the kernel support changes, leading to a jump in Z_h^2 and, therefore, in $E_{\min}$. This effect becomes negligible for larger c and larger r_c. We also observe that $E_{\min}$ of the uncorrected operators increases with increasing order r. This is confirmed by results for order $r = 6$ (not shown). The DC operators theoretically yield the desired rate of convergence for all orders and resolutions. The condition number of the linear system of equations (Eq. (9)), however, increases with increasing c and r. For $r = 6$ and $c = 1.4$, Gauss elimination with partial pivoting is not sufficient any more and pre-conditioning might become necessary.

We also compare the DC PSE operators to the corresponding limiting FD stencils (solid lines in Fig. 1). For $r = 2$, these are obtained for $c \to \infty$ (see Section 3) and for $r = 4$ for $r_c = 2h$ and $c = 1$. The error of the FD stencils mostly coincides with that of the DC PSE operators for $c = 1.4$, where the DC PSE operators effectively have the same support as the FD stencils.

4.1.2. Computational efficiency

We quantify the computational efficiency of the operators through the computational cost needed to reach a certain error level. Table 1 reports the computational costs for the two-dimensional Eulerian advection case described in Appendix C. We report the CPU time required for a single evaluation of the operators on all the particles (t_1) and the total time needed to reach an L_2 error of <1% of the initial pulse height in the whole domain at final time $T = 0.5$ (t_{all}). All timings were done using MATLAB 7.6.0.324 (R2008a) on a 2 GHz Intel Core Duo processor with 1 GB RAM. For all operators, we convolve the square matrix of precomputed kernel weights with the square matrix of field values f at the particle locations. As an implementation- and machine-independent measure, we also list the ratio $N = k/h^2$, where k is the number of neighbor particles (non-zero entries in the stencil). The time $t_1(N)$ is expected to be in $\mathcal{O}(N)$.

For uncorrected operators with $c = 0.55$, t_{all} decreases considerably with increasing order r, as already reported by Eldredge et al. [1]. This is true despite the fact that the cutoff radius increases from $r_c = 3.5\varepsilon$ to 5.5ε when going from $r = 2$ to $r = 4$. Increasing c to 0.9 for uncorrected operators leads to higher efficiency since the number of neighbors within the fixed cutoff radius $r_c = 3.5\varepsilon$ decreases. As shown in Fig. 1, however, convergence of such operators is impaired.

Table 1 reveals that the computational efficiency of DC PSE operators is always higher than the one of the corresponding uncorrected operators. Furthermore, increasing c for DC operators improves their efficiency (through reducing k) without hampering convergence. In the limit $c \to \infty$, we recover the classical compact FD stencil as the most efficient operator. Compact FD stencils involve the least number of neighbors k at full accuracy and rate of convergence. They do, however, also provide the lowest amount of regularization on noisy or discontinuous fields.

Table 1
CPU time needed for solving the two-dimensional test case of Appendix C on uniform Cartesian particle distributions to a final error of 1%. The time t_1 is required for a single evaluation of the operator on all the particles, whereas t_{all} is the time needed to reach the target error level of 1%. The computational cost is governed by the implementation-independent ratio $N = k/h^2$, where k is the number of particles within the kernel support (non-zero entries in the stencil) and h the interparticle spacing.

Kernel type	c	r	r_c	N	t_1 in ms	t_{all} in s
Uncorrected operator	0.55	2	3.5ε	6,611,570	329.	82.5
Uncorrected operator	0.90	2	3.5ε	840,145	37.7	5.77
DC operator	0.55	2	2ε	1,974,145	86.2	20.2
DC operator	0.90	2	2ε	165,035	15.3	1.98
DC operator	1.40	2	2ε	68,787	4.32	0.445
FD stencil		2		29,210	3.79	0.360
Uncorrected operator	0.55	4	5.5ε	1,211,890	66.5	16.3
Uncorrected operator	0.90	4	5.5ε	219,074	12.9	1.50
DC operator	0.55	4	3ε	304,978	15.6	3.10
DC operator	0.90	4	3ε	50,013	3.61	0.321
DC operator	1.40	4	3ε	11,464	1.50	0.0932
FD stencil		4		7643	1.51	0.0937

4.2. Irregular particle distributions

We assess the rate of convergence and computational efficiency of DC PSE operators on irregular particle distributions. In order for the linear system (Eq. (9)) to be fully determined, each particle must have at least $k_{\min} = m$ neighbors, where m is the number of different multiindices $\boldsymbol{\alpha} \in \mathbb{N}^n$ with $|\boldsymbol{\alpha}| = \alpha_{\min}, \ldots, |\boldsymbol{\beta}| + r - 1$ (see Eq. (7)). All results presented in this section are obtained using the kernel function template given in Eq. (8).

4.2.1. Rate of convergence

We consider the convergence of the relative error when approximating the first derivative along x of the two-dimensional Gauss pulse

$$f(x,y) = \frac{1}{\pi\sigma^2} e^{-\frac{(x-x_0)^2+(y-y_0)^2}{\sigma^2}}, \quad \sigma = 0.1, \tag{24}$$

at position $\boldsymbol{x} = (x_0 + \sigma, y_0)$ using DC PSE operators of orders $r = 2, 4, 6$ on four different irregular distributions. The ratio $c = h/\varepsilon$ is kept constant at $c = \{0.5, 0.9, 1.4\}$, while the particle arrangements are scaled according to the desired resolution. The particle volumes are set to the average volume h^2. In real-world applications where particle volumes evolve according to the flow field, better estimates can be used.

The results are summarized in Fig. 2. It can be seen that the uncorrected operators diverge due to discretization errors whereas the DC PSE operators yield the desired rate of convergence in all cases. For $r = 6$, an error term of order $s = -1$ (Eq. (5)) dominates at high resolutions, due to numerical inaccuracies when computing the coefficients $a_\gamma(\boldsymbol{x})$. This underlines the importance of satisfying the discrete moment conditions as accurately as possible.

4.2.2. Computational efficiency

On irregular particle distributions, the DC kernel function $\eta^\beta(\boldsymbol{z})$ becomes a field of kernel functions, $\eta^\beta(\boldsymbol{z}, \boldsymbol{x})$, thus requiring the solution of a different linear system of equations for each position $\boldsymbol{x}$ where the operator is to be evaluated (see Section 2). Moreover, the kernels have to be recomputed whenever the particles have moved. The computational cost then becomes comparable to that of the vorticity redistribution method [31] or the discrete PSE scheme for the diffusion step in vortex methods proposed by Poncet [10]. For a detailed discussion of the computational cost of DC PSE operators on moving particles, we refer to Section 4.4.

If the particle distribution is not arbitrary, but the result of a known convective velocity field, the kernels need not necessarily be recomputed at every time step, but can be adapted based on the known velocity. Starting from the initial particle distribution and the corresponding DC PSE operators, one can define a mapping from the old to the new particle positions. The operators can then be adapted in analogy to the variable vortex blob method [32,33]. For non-linear mappings, however, additional error terms appear. For high orders of accuracy, we thus expect velocity-based operator adaptation to be computationally more expensive than reinitializing the particles at every time step.

4.3. Boundary effects

The accuracy of uncorrected full-space PSE operators usually deteriorates near boundaries of the computational domain. Eldredge et al. [1] therefore derived one-sided integral operators with significantly improved accuracy near boundaries. Such a special treatment is not necessary when using DC PSE operators since they do not rely on regularity or symmetry of the particle distribution. The skewed particle distributions near boundaries are simply treated as irregular particle distributions and the corresponding DC PSE operators are constructed by solving the resulting linear systems of equations.

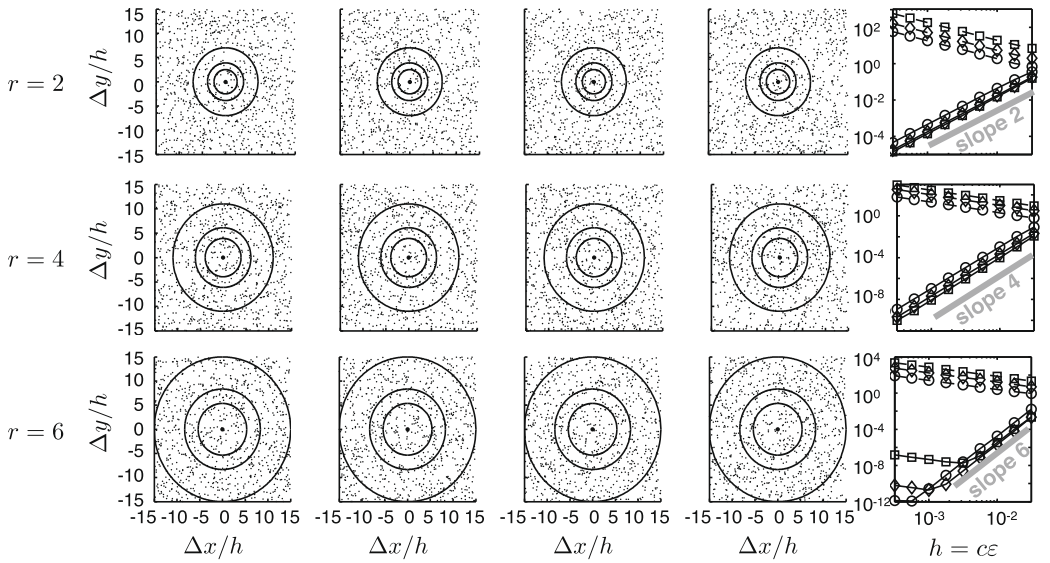

Fig. 2. Convergence of DC PSE operators (solid lines) and of uncorrected PSE operators (dashed lines) of order $r = 2, 4, 6$ (top to bottom) on random particle distributions. The right panels show the maximum of the relative error when approximating the first derivative of the Gauss pulse in Eq. (24) at the center particles of four random particle distributions for $c = 0.5$ (○), $c = 0.9$ (◇) and $c = 1.4$ (□). The considered particle distributions, with center particles at positions $\boldsymbol{x} = (x_0 + \sigma, y_0)$, are shown in the four panels on the left. The circles show the support of the operators for the different values of c. The cutoff radii are $r_c = 3.5\varepsilon, 5.5\varepsilon, 7.5\varepsilon$ for $r = 2, 4, 6$, respectively.

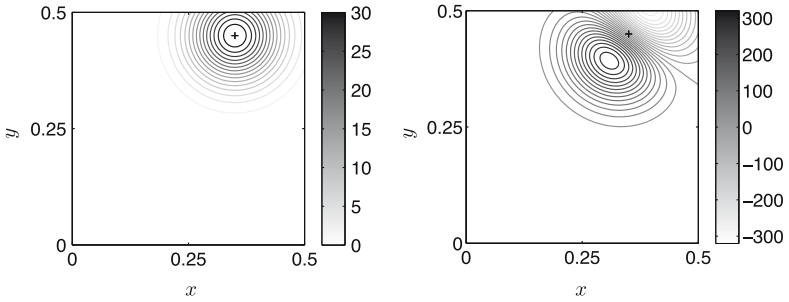

Fig. 3. The test case used to assess the convergence of the operators near boundaries. The left panel shows the contour lines of a Gauss pulse (Eq. (24)) centered at $(x_0, y_0) = (0.35, 0.45)$ in a domain $[0, 0.5]^2$. The right panel shows the contour lines of the analytical solution of the directional derivative along $\boldsymbol{d} = (0.588, 0.809)$. The + marks the center of the pulse.

We demonstrate that the presence of boundaries does not affect the order of accuracy of DC PSE operators by considering a two-dimensional Gauss pulse (Eq. (24)) leaving the computational domain through an absorbing boundary (Fig. 3). Convergence of the resulting relative errors is shown in Fig. 4 for uncorrected full-space, uncorrected one-sided, and DC PSE operators approximating the directional derivative $\boldsymbol{d} \cdot \nabla f$ of the Gauss pulse centered at $(x_0, y_0) = (0.35, 0.45)$ in a computational domain of size $[0, 0.5]^2$ (Fig. 3). For the one-sided uncorrected operators, we only consider particles in the upwind direction of $\boldsymbol{d}$. It can be seen from Fig. 4 that the uncorrected full-space operators diverge in all cases (dominating error of order $s = -1$) and should not be used near boundaries. The uncorrected one-sided operators show constant L_∞ errors (bottom row of panels) for orders $r = 1$ to $r = 3$ and diverge for $r = 4$. The DC PSE operators yield the desired rates of convergence in both the L_2 (upper panels) and the L_∞ norms until numerical inaccuracies in the determination of the kernel coefficients start to dominate the error ($r = 4$ with $c = 1.4$, solid line with square symbols).

Fig. 5 visually compares the solution obtained using uncorrected one-sided operators and DC PSE operators of orders $r = 1$ and $r = 3$. The example shown is computed using $h = 0.01$ and $c = 0.55$. It can be seen that the uncorrected operators lead to distortions and kinks in the iso-lines near boundaries, preventing convergence of the L_∞ error.

4.4. A Lagrangian advection–diffusion test case

We demonstrate the use of DC PSE operators in a more complex test case with moving particles: a two-dimensional Lagrangian advection–diffusion simulation. Again, we compare the DC PSE operators with uncorrected PSE operators and

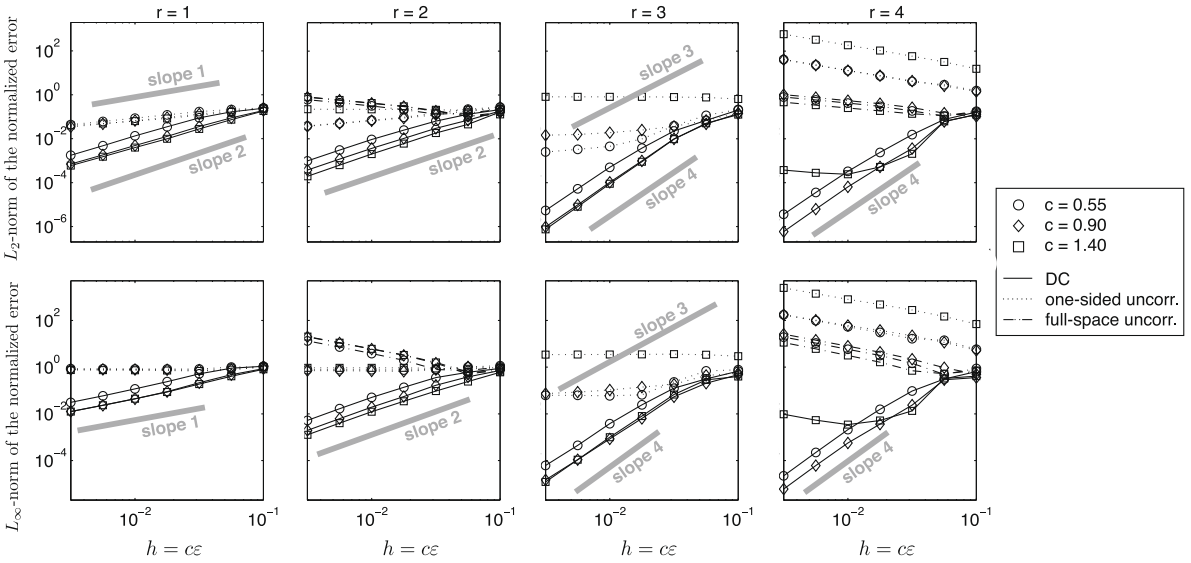

Fig. 4. Convergence of the uncorrected full-space, uncorrected one-sided, and DC PSE operators approximating the directional derivative of the Gauss pulse shown in Fig. 3. We show convergence of both the L_2 (top row of panels) and L_∞ norms of the relative errors for operators of design orders $r = 1, 2, 3, 4$ (left

finite differences. Details of the test case and the numerical schemes are described in Appendix B. We assess the computational cost of DC PSE operators by measuring the CPU times of simulations for the Péclet numbers Pe = {1, 10, 100, 1000} to final relative errors of less than {0.1%,0.05%,0.05%,0.1%}, respectively. These error levels are chosen such that they can be reached also with uncorrected operators (see Section 4.1.1). We only test second-order accurate operators. The particles are either remeshed to regular Cartesian positions at every time step, or they are never remeshed. The latter is possible because the velocity field does not lead to holes in the particle distribution. FD stencils are evaluated using the connectivity information of the mesh, whereas the PSE simulations use neighbor lists (we use Verlet lists [34]) even if remeshing is done at every time step. In all cases, the Verlet lists are recomputed at every time step.

We show the convergence plots for Péclet numbers 1 and 1000 in Fig. 6. All results are summarized in Table 2. As expected, Eulerian FD show the best computational efficiency for low Péclet numbers. For high Péclet numbers (100 and 1000), Lagrangian methods are more efficient. In all cases, DC PSE operators are more efficient than uncorrected ones. DC PSE operators can also outperform Lagrangian FD (see Appendix B.3.3) at high Péclet numbers (100 and 1000) since they do not require remeshing. If remeshing is done at every time step, FD stencils are preferable. The larger the Péclet number, however, the more the remeshing error dominates over the error introduced by the diffusion operator. This can be seen by comparing the resolution h that is required to reach the target error level.

On irregular particle distributions (i.e., without remeshing), DC operators require that the correction function is recomputed for each particle at every time step. This additional computational cost accounts for 85–90% of the total CPU time. It is, however, amortized by the gain in accuracy (the target error level can be reached with coarser resolution) of DC operators in all cases except Pe = 1. This coarser resolution also allows larger time steps. In cases where the advection error dominates, higher resolution might therefore again be required, making DC PSE operators less efficient.

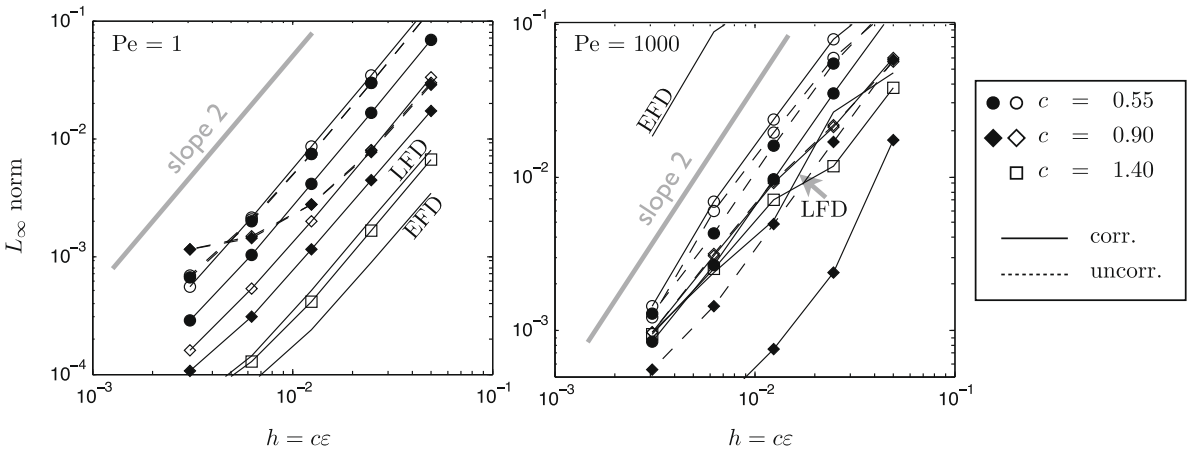

Fig. 6. Convergence plots for the advection–diffusion simulation for Pe = 1 (left) and Pe = 1000 (right). Empty markers denote simulations with remeshing, while filled markers denote simulations without remeshing. The FD simulations are shown as solid lines without markers. LFD refers to Lagrangian FD and EFD to Eulerian FD.

Table 2
CPU time t_{CPU} (in seconds) and interparticle spacing (or mesh resolution) h required for solving the two-dimensional advection–diffusion problem described in Appendix B for Pe = {1, 10, 100, 1000} with a relative error of {0.1% , 0.05%, 0.05%, 0.1%}, respectively. We compare DC PSE operators ("DC") with uncorrected ones ("UC") and FD for $r = 2$ and $\Delta t \lesssim 0.15h^2$Pe. Values are based on interpolations from simulations with $h \in \{3.125, 6.25, 12.5, 25.0, 50.0\} \cdot 10^{-3}$.

	op.	c	r_c	Pe = 1		Pe = 10		Pe = 100		Pe = 1000	
				$10^3 h$	t_{CPU}	$10^3 h$	t_{CPU}	$10^3 h$	t_{CPU}	$10^3 h$	t_{CPU}
Remeshing	UC	0.55	3.5ε	3.99	36,300	4.85	5020	5.18	583.	2.87 [a]	739.[a]
	UC	0.90	3.5ε	2.07[a]	21,300[a]	4.86	2160	5.40	213.	3.18	203.
	DC	0.55	2ε	4.27	10,900	4.89	2077	5.09	274.	2.67[a]	405.[a]
	DC	0.90	2ε	8.74	256.	7.34	191.	5.30	121.	3.20	89.1
	DC	1.40	2ε	19.5	6.87	7.60	120.	5.24	86.3	3.24	69.4
No remeshing	UC	0.55	3.5ε	4.10	31,600	5.02	4280	5.73	381.	2.73[a]	915.[a]
	UC	0.90	3.5ε	2.24[a]	144,000[a]	7.72	289.	10.2	13.9	4.79	37.1
	DC	0.55	2ε	6.17	10,100	7.29	1600	7.55	210.	3.50	533.
	DC	0.90	2ε	11.7	533.	15.6	53.1	23.9	1.49	14.9	1.21
Lagrangian FD				17.6	0.716	6.80	11.0	4.55	8.70	3.22	4.41
Eulerian FD				26.8	<0.02	9.80	0.268	2.37[a]	16.7[a]	0.883[a]	41.0[a]

[a] Value based on extrapolation.

5. Wavenumber modification: implications for numerical dispersion, numerical diffusion, and stability

We quantify the wavenumber modifications introduced by the operators. Wavenumber modifications manifest themselves as numerical dispersion and numerical diffusion. We analyze the wavenumber modifications of DC PSE operators in three one-dimensional test cases: the linear wave equation, the convection equation, and the diffusion equation. Based on the modified wavenumbers, we provide closed-form stability conditions for DC PSE operators in continuous and discrete time.

5.1. Linear wave equation and convection equation

We derive the wavenumber modification relations $k_{\text{mod}}(k)$ of DC PSE operators for the one-dimensional linear wave equation

$$\frac{\partial^2 f}{\partial t^2} - u^2 \frac{\partial^2 f}{\partial x^2} = 0, \tag{25}$$

and the one-dimensional convection equation

$$\frac{\partial f}{\partial t} + u \frac{\partial f}{\partial x} = 0 \tag{26}$$

for speeds $u > 0$.

In order to derive expressions for the wavenumber modification, we compare the dispersion relation $\omega(k)$ of a traveling wave $e^{i(kx-\omega t)}$ obeying the original equation (Eq. (25) or Eq. (26), respectively) with the dispersion relation obtained when the spatial derivatives are approximated by a PSE operator (Eq. (3)). If the wave $e^{i(kx-\omega t)}$ is a solution to the original problem, then $e^{i(k_{\mathrm{mod}}(k)x-\omega t)}$ solves the spatially discretized equation. For irregular particle distributions, the wavenumber modification depends on the position x.

For the wave equation (Eq. (25)), we find the following relation between the original wavenumbers and the modified ones:

$$k_{\mathrm{mod}}(k) = \frac{1}{\varepsilon}\sqrt{Z_h^0(x) - \hat{\eta}_x^{(2)}(k\varepsilon)}, \tag{27}$$

where $\hat{\eta}_x^{\beta}(k\varepsilon)$ is defined as a non-uniform analog of the discrete Fourier transform of the kernel η^{β} centered at x, hence,

$$\hat{\eta}_x^{\beta}(k\varepsilon) = \sum_{p\in\mathcal{N}(x)} v_p e^{-\hat{\imath}k(x-x_p)}\eta_{\varepsilon}^{\beta}(x-x_p, x).$$

Z_h^0 is the zeroth discrete moment of the kernel $\eta^{(2)}$ as defined in Eq. (6). Taylor-expanding $\hat{\eta}_x^{(2)}$ around $k\varepsilon = 0$ and substituting into Eq. (27) yields

$$k_{\mathrm{mod}}(k) = k\left[\sum_{\alpha=1}^{\infty}\frac{(-\hat{\imath}k\varepsilon)^{\alpha-2}}{\alpha!}Z_h^{\alpha}(x)\right]^{1/2}. \tag{28}$$

For the one-dimensional convection equation (Eq. (26)), the modified wavenumber is

$$k_{\mathrm{mod}}(k) = -\frac{\hat{\imath}}{\varepsilon}\left[Z_h^0(x) + \hat{\eta}_x^{(1)}(k\varepsilon)\right].$$

After Taylor-expanding around $k\varepsilon = 0$, this becomes

$$k_{\mathrm{mod}}(k) = k\left[-\sum_{\alpha=0}^{\infty}(\delta_{\alpha 0}+1)\frac{(-\hat{\imath}k\varepsilon)^{\alpha-1}}{\alpha!}Z_h^{\alpha}(x)\right], \tag{29}$$

where δ_{ij} is the Kronecker delta, and the Z_h^{α} are the αth discrete moments of the kernel $\eta^{(1)}$.

For symmetric particle distributions with even kernel functions η^{β} and even β, or with odd kernel functions η^{β} and odd β, the discrete moments Z_h^{α} are zero for all odd $\alpha-\beta$. The effect of the wavenumber modification is thus purely dispersive in these cases. For non-symmetric particle distributions, there may be non-zero moments Z_h^{α} for odd $\alpha-\beta$, introducing diffusive terms. The modified wavenumbers then contain imaginary parts that indicate position-dependent amplitude changes. This changes the shape of the original wave, analogously to a diffusion process. For even β, the diffusive terms are typically small compared to the dispersive terms. This is because the first discrete moments Z_h^{α} that are non-zero by design are the moments Z_h^{β} and $Z_h^{\beta+r}$.

5.1.1. Results on uniform cartesian particle distributions

On Cartesian particle distributions, the uniform interparticle spacing h limits the spectrum to $k \leqslant \pi/h$ (Nyquist–Shannon sampling theorem). We therefore restrict our analysis to the interval $k \in [0, \pi/h]$.

Fig. 7 shows the wavenumber modification for the wave equation (Eq. (25)) and the convection equation (Eq. (26)), both for uncorrected and DC PSE operators for $c = 0.5, c = 0.9$, and $r = 2, 4, 6, 8$. For the DC PSE operators, the kernel template given in Eq. (23) is used. For second-order operators ($r = 2$), the curves for uncorrected and DC operators are indistinguishable. For higher orders of accuracy, the DC operators have smaller modifications of the wavenumbers than the uncorrected ones. DC operators thus have lower numerical dispersion than uncorrected PSE operators over the entire range of wavenumbers. Also, the wavenumber modifications decrease with increasing order of accuracy and increasing c, both for DC and uncorrected operators.

The effect of numerical dispersion is further illustrated for a two-dimensional advection problem in Appendix C. As expected from the one-dimensional case discussed above, both the order of accuracy r and the ratio c influence the dispersive properties of the operators. Since dispersion decreases with increasing c, DC operators can be made much less dispersive than uncorrected ones as they allow larger values of c at full rate of convergence (see Section 4.1).

5.1.2. Results on irregular particle distributions

On irregular (asymmetric) particle distributions, the modified wavenumbers contain imaginary parts that lead to numerical diffusion. Figs. 8 and 9 show the real and imaginary parts of the modified wavenumbers for the wave equation (Eq. (25)) and the convection equation (Eq. (26)), respectively. We compare uncorrected and DC (kernel template of Eq. (8)) PSE operators evaluated on the center particle of 10,000 random particle distributions for $c = 0.5$ and $c = 0.9$. We report the medians (lines) and the areas covered by the central 68.2% of all curves $k_{\mathrm{mod}}(k)$ (shaded bands). The particle distributions are generated as follows: We subdivide the operator support $[-r_c, r_c]$ into equisized cells of width h and place one particle per cell. The position of each particle inside its cell is sampled from a uniform probability distribution. Particle distributions that lead to

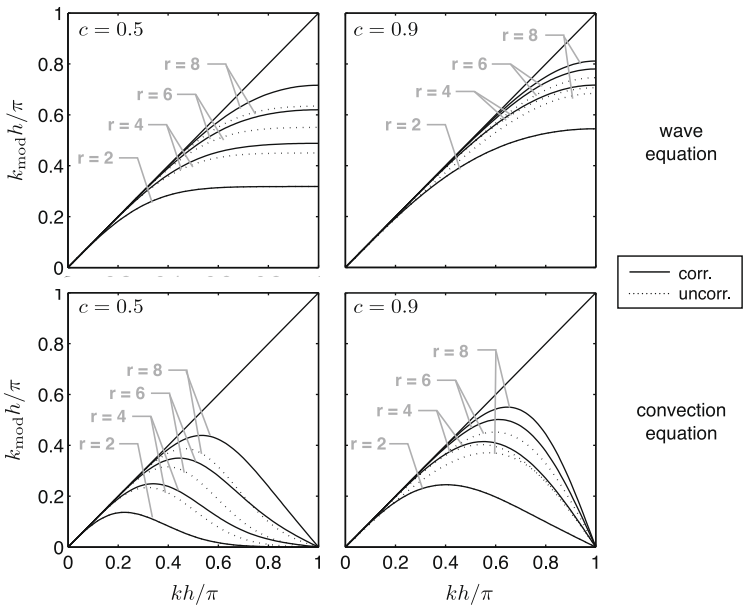

Fig. 7. Wavenumber modification on uniform Cartesian particle distributions. The modified wavenumbers k_{mod} of the solutions of the one-dimensional wave equation (top) and the one-dimensional convection equation (bottom) are shown for DC (solid lines) and uncorrected (dotted lines) PSE operators of orders $r = 2, 4, 6, 8$ and $c = 0.5$ (left) and $c = 0.9$ (right).

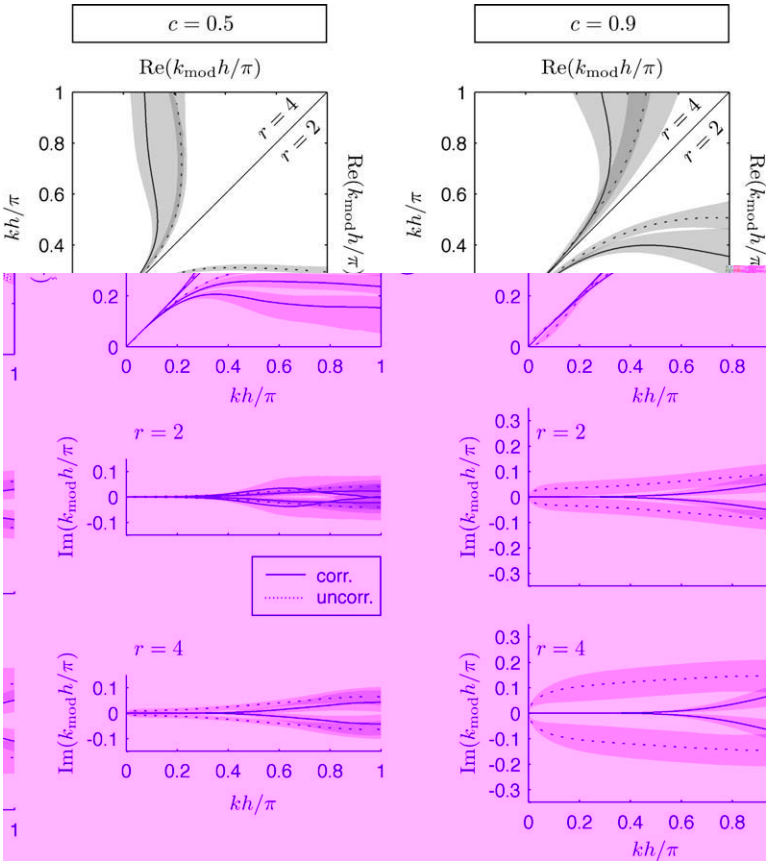

Fig. 8. Wavenumber modification for the wave equation on random particle distributions. The real and imaginary parts of the modified wavenumbers k_{mod} are shown for DC and uncorrected PSE operators of order $r = 2$ and $r = 4$ for $c = 0.5$ (left) and $c = 0.9$ (right). Each experiment is repeated for 10,000 random particle distributions. The lines report the median and the shaded areas the central 68.2% of the resulting curves.

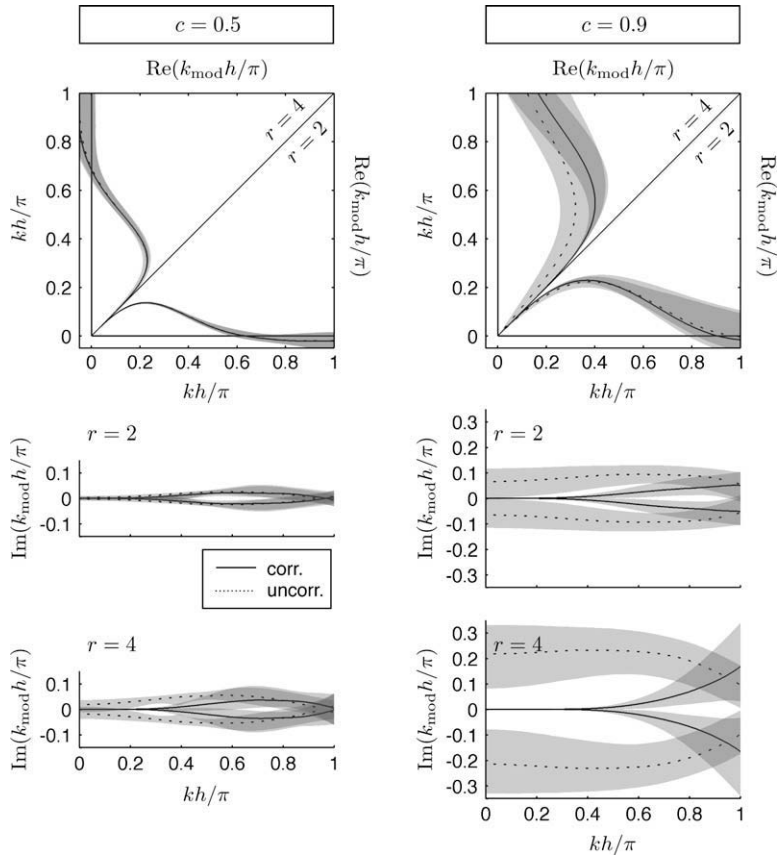

Fig. 9. Wavenumber modification for the convection equation on random particle distributions. The real and imaginary parts of the modified wavenumbers k_{mod} are shown for DC and uncorrected PSE operators of order $r = 2$ and $r = 4$ for $c = 0.5$ (left) and $c = 0.9$ (right). Each experiment is repeated for 10,000 random particle distributions. The lines report the median and the shaded areas the central 68.2% of the resulting curves.

linear systems of equations with condition numbers above a certain threshold are resampled. According to the generalized sampling theorem for non-uniform sampling [35], we use the average interparticle spacing as the characteristic h, again limiting the spectrum of wavenumbers to $k \leqslant \pi/h$.

As in the uniform case, the modification of the real part decreases with increasing r and c. For the wave equation (Fig. 8), the uncorrected operators lead to smaller modifications in $\mathrm{Re}(k)$ than the DC operators. For the convection equation (Fig. 9), however, DC operators show comparable or lower numerical dispersion than uncorrected ones. The imaginary parts (leading to numerical diffusion) are always smaller for DC operators than for uncorrected ones for wavenumbers $k \lesssim c\pi/h$.

For $c = 0.5$ and $r = 2$ on the wave equation (Fig. 8, left), $\mathrm{Re}(k_{\mathrm{mod}}(k))$ of DC operators splits into two curves. The upper curve results from all operators with strictly non-negative kernel functions (83% of the random distributions tested). In this case, non-negative kernels hence lead to less numerical dispersion. The effect on numerical diffusion is, however, negligible.

5.2. Diffusion equation

For the one-dimensional diffusion equation

$$\frac{\partial f}{\partial t} - v\frac{\partial^2 f}{\partial x^2} = 0, \tag{30}$$

the dispersion relation is $\omega(k) = -\hat{\imath}vk^2$, where $v > 0$ is the viscosity (or diffusion constant). The modified dispersion relation $\omega_{\mathrm{mod}}(k) = -\hat{\imath}vk_{\mathrm{mod}}(k)^2$ leads to the same modified wavenumber (Eq. (28)) as for the wave equation. Alternatively, the modification can also be absorbed into the viscosity as $\omega_{\mathrm{mod}}(k) = -\hat{\imath}v_{\mathrm{mod}}(k)k^2$. This leads to the modified viscosity

$$v_{\mathrm{mod}}(k) = \frac{v}{(k\varepsilon)^2}\left[Z_h^0(x) - \hat{\eta}_x^{(2)}(k\varepsilon)\right] = v\sum_{\alpha=1}^{\infty}\frac{(-\hat{\imath}k\varepsilon)^{\alpha-2}}{\alpha!}Z_h^{\alpha}(x).$$

For non-uniform particle distributions the modified viscosity depends on the position x. $\mathrm{Re}(v_{\mathrm{mod}})/v > 1$ results in overdiffusion and $\mathrm{Re}(v_{\mathrm{mod}})/v < 1$ in underdiffusion. The effect of the imaginary part of the modified viscosity is both dispersive and diffusive.

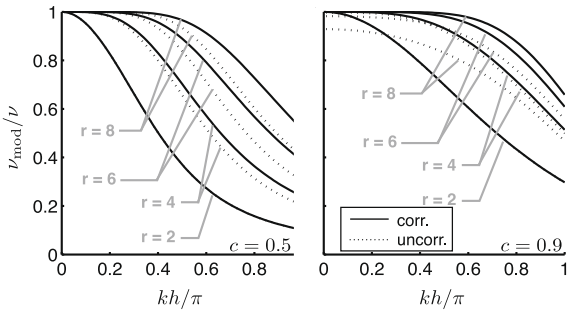

Fig. 10. Viscosity modification for the diffusion equation on uniform Cartesian particle distributions. The ratio of the modified viscosity to the true viscosity v_{mod}/v is shown for DC and uncorrected PSE operators of order $r = 2, 4, 6, 8$ for $c = 0.5$ (left) and $c = 0.9$ (right).

5.2.1. Results on uniform cartesian particle distributions

Fig. 10 shows v_{mod}/v versus kh/π for operators with $c = 0.5$ and $c = 0.9$ on uniform Cartesian particle distributions. All operators lead to increasing underdiffusion for increasing wavenumbers. For DC operators (kernel template of Eq. (23)), however, the modified viscosity v_{mod} is closer to the true viscosity v than for uncorrected operators. Also, increasing r or c leads to less underdiffusion for DC operators. For uncorrected operators, high r and c lead to underdiffusion even at $kh \to 0$ due to the constant discretization error.

5.2.2. Results on random particle distributions

On non-uniform particle distributions, the modified viscosity is complex. Fig. 11 shows its real and imaginary parts for DC (kernel template of Eq. (8)) and uncorrected operators. We show the medians and the areas covered by the central 68.2% of all curves $v_{\mathrm{mod}}(k)/v$ for 10,000 random particle distributions as described in Section 5.1.2.

While uncorrected operators show less underdiffusion for larger wavenumbers, they do not reproduce the correct viscosity in the limit $kh \to 0$; their imaginary part approaches infinity and there is a bias in the real part. This inconsistency results from the discretization error. The effect becomes worse with increasing r and c.

5.3. Stability

Numerical stability requires that small perturbations, such as round-off errors, decay over time. If the effect $\delta f(t)$ of an error δf_0, introduced at time t_0, can be bounded by $|\delta f(t)| \leqslant e^{\lambda(t-t_0)}|\delta f_0|$ with exponent $\lambda < 0$, the system is called exponentially stable. Typically, the amplification of each Fourier mode of δf_0 can be bounded separately by a wavenumber-dependent exponent $\lambda_{\boldsymbol{k}}$. Stability is then determined by $\lambda = \max_{\boldsymbol{k}} \lambda_{\boldsymbol{k}}$.

We consider the stability of numerical solutions of partial differential equations of order $|\boldsymbol{\beta}|$ in space and a in time,

$$\frac{\partial^a f}{\partial t^a} = bD^{\boldsymbol{\beta}} f, \tag{31}$$

with periodic boundary conditions. We distinguish two cases: (1) the continuous-time case where the spatial derivative $D^{\boldsymbol{\beta}} f$ is replaced by the PSE approximation $Q_h^{\boldsymbol{\beta}} f$, and (2) the discrete-time case, where in addition the time derivative is approximated by finite differences. For the continuous-time case we derive the exponents $\lambda_{\boldsymbol{k}}$ in terms of the modified wavenumbers. For the discrete-time case we provide CFL conditions for different time-stepping schemes.

5.3.1. Continuous time

The modified wave $e^{\hat{\imath}(\boldsymbol{k}_{\mathrm{mod}}\cdot\boldsymbol{x}-\omega t)}$ satisfying Eq. (31) when $D^{\boldsymbol{\beta}} f$ is replaced with $Q_h^{\boldsymbol{\beta}} f$ can be rewritten as

$$e^{\hat{\imath}(\boldsymbol{k}_{\mathrm{mod}}\cdot\boldsymbol{x}-\omega t)} = e^{\mathrm{Re}\{[b(\hat{\imath}\boldsymbol{k}_{\mathrm{mod}}(\boldsymbol{k}))^{\boldsymbol{\beta}}]^{1/a}\}t} e^{\hat{\imath}(\boldsymbol{k}\cdot\boldsymbol{x}-\mathrm{Im}\{[b(\hat{\imath}\boldsymbol{k}_{\mathrm{mod}}(\boldsymbol{k}))^{\boldsymbol{\beta}}]^{1/a}\}t)}.$$

The amplitude of the modified wave thus is $e^{\lambda_{\boldsymbol{k}} t}$ with

$$\lambda_{\boldsymbol{k}} = \mathrm{Re}\{[b(\hat{\imath}\boldsymbol{k}_{\mathrm{mod}}(\boldsymbol{k}))^{\boldsymbol{\beta}}]^{1/a}\} = \begin{cases} \mathrm{Re}\left\{\left[\frac{b}{\hat{\imath}^{|\boldsymbol{\beta}|}} \sum_{|\boldsymbol{\alpha}|=1}^{\infty} \frac{(-\hat{\imath}\varepsilon\boldsymbol{k})^{\boldsymbol{\alpha}}}{\boldsymbol{\alpha}!} Z_h^{\boldsymbol{\alpha}}(\boldsymbol{x})\right]^{1/a}\right\} & |\boldsymbol{\beta}| \text{ even} \\ \mathrm{Re}\left\{\left[\frac{b}{\hat{\imath}^{|\boldsymbol{\beta}|}} \sum_{|\boldsymbol{\alpha}|=0}^{\infty} (1+\delta_{|\boldsymbol{\alpha}|0}) \frac{(-\hat{\imath}\varepsilon\boldsymbol{k})^{\boldsymbol{\alpha}}}{\boldsymbol{\alpha}!} Z_h^{\boldsymbol{\alpha}}(\boldsymbol{x})\right]^{1/a}\right\} & |\boldsymbol{\beta}| \text{ odd.} \end{cases}$$

Of the a roots of the term $[\cdot]^{1/a}$, the one with maximum real part is chosen. On a particle distribution of resolution h, the maximum exponent λ is the maximum over all $\lambda_{\boldsymbol{k}}$ with $|\boldsymbol{k}|h \in]0, \sqrt{n}\pi]$. For the one-dimensional wave equation (Eq. (25)), convection equation (Eq. (26)), and diffusion equation (Eq. (30)), the wavenumber-dependent exponents are

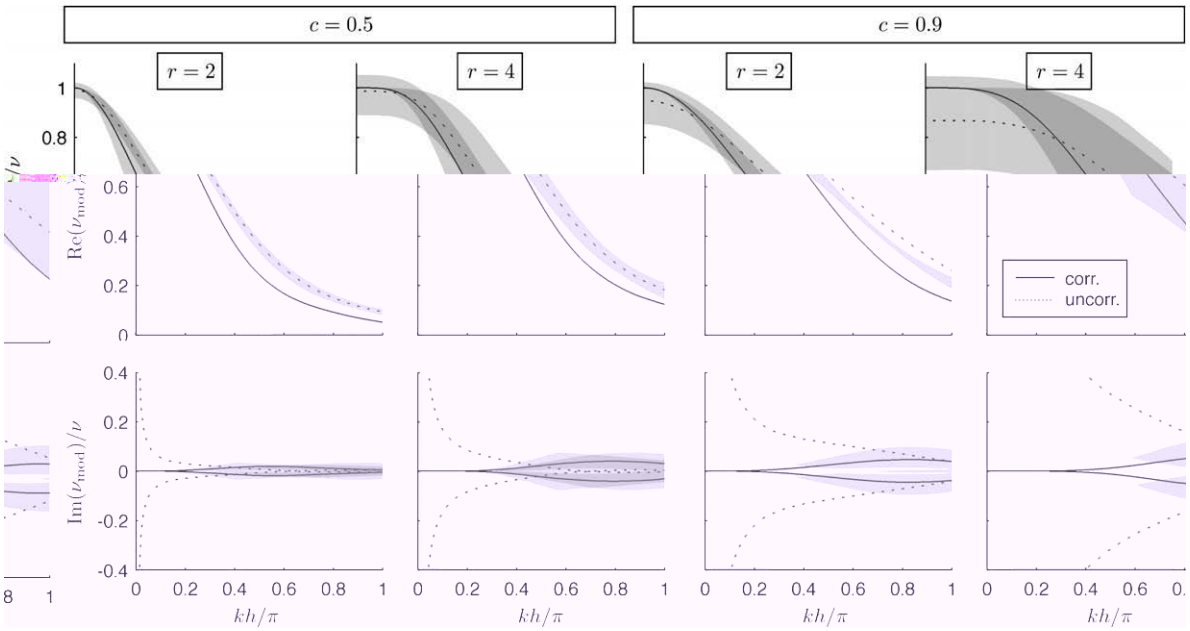

Fig. 11. Viscosity modification for the diffusion equation on random particle distributions. The real and imaginary parts of ν_{mod}/ν are shown for DC and uncorrected PSE operators of order $r = 2$ and $r = 4$ for $c = 0.5$ (left) and $c = 0.9$ (right). Each experiment is repeated for 10,000 random particle distributions. The lines report the median and the shaded areas the central 68.2% of the resulting curves.

$$\lambda_k^{\text{wave}} = u|\text{Im}(k_{\text{mod}}(k))|, \tag{32}$$

$$\lambda_k^{\text{conv}} = u\ \text{Im}(k_{\text{mod}}(k)), \tag{33}$$

$$\text{and} \quad \lambda_k^{\text{diff}} = \nu[\text{Im}(k_{\text{mod}}(k))^2 - \text{Re}(k_{\text{mod}}(k))^2], \tag{34}$$

respectively. To simplify notation, we will not always explicitly state the dependency of k_{mod} on k in the following.

Using the expressions for the modified wavenumbers presented above, these exponents imply that on uniform Cartesian particle distributions all operators are exponentially stable for the diffusion equation and neutrally stable ($\lambda_k = 0$, neither error amplification nor decay) for the wave equation and the convection equation. Neutral stability is all that can be achieved using centered operators on the hyperbolic wave and convection equations. Exponential stability on these equations would require upwind schemes.

On irregular particle distributions, all operators lead to instabilities for the wave equation, due to the imaginary part of the modified wavenumber. For the convection equation, most operators result in $\text{Im}(k_{\text{mod}}) > 0$ for some $kh \in]0, \pi]$ and are thus unstable. For the diffusion equation, uncorrected operators are exponentially stable on all, and DC operators on 98%, of the 10,000 randomly generated particle distributions. On 2% of the particle distributions, DC operators led to instabilities. Our results, however, suggest that this is the case only for $c > c_{\text{max}}$, where the critical value c_{max} depends on the degree of Lagrangian grid distortion. We test this by considering particle distributions that are perturbations of uniform Cartesian distributions. Regularly placed particles with spacing h are perturbed by adding uniform random numbers in $[-\xi/2, \xi/2]$ to their positions. This mimics Lagrangian grid distortion in simulations where the particles are periodically remeshed. The parameter ξ quantifies the degree of distortion. Table 3 lists the critical c_{max} for different ξ for kernels with three different additional conditions on the zeroth-order moment. For each $\xi \in \{0.1, 0.2, \ldots, 1.5\}$, we report the maximum c for which no instabilities

Table 3
Critical c, c_{max}, for stability of second-order DC PSE operators on the diffusion equation as a function of the degree of Lagrangian grid distortion ξ. We show the results for the additional moment condition $Z_h^0 = \{0, 5, 10\}$.

ξ/h	0.1	0.2	0.3	0.4	0.5	0.6	0.7	0.8	0.9	1.0	1.1	1.2	1.3	1.4	1.5
$Z_h^0 = 0$: c_{max}	3.4	3.3	3.2	3.1	3.0	2.9	2.8	0.0	0.0	0.0	0.0	0.0	0.0	0.0	0.0
$Z_h^0 = 5$: c_{max}	3.4	3.3	3.2	3.1	3.0	2.9	2.8	1.0	0.9	0.7	0.7	0.7	0.6	0.6	0.6
$Z_h^0 = 10$: c_{max}	3.4	3.3	3.2	3.1	3.0	2.9	2.8	1.0	0.8	0.3	0.2	0.2	0.2	0.2	0.2

Table 4
Wavenumber-based stability conditions for different time discretization schemes and equations. We write $\min_k$ ($\max_k$) for $\min_{k\in]0,\pi/h|}$ ($\max_{k\in]0,\pi/h|}$).

Exponential stability with first-order FT time discretization	
Convection eq.	$\Delta t < \min_k - 2\mathrm{Im}(k_{\mathrm{mod}})/(u\lvert k_{\mathrm{mod}}\rvert^2) = -\lambda^*_{\mathrm{conv}} h/u$
Diffusion eq.	$\Delta t < \min_k 2[\mathrm{Re}(k_{\mathrm{mod}})^2 - \mathrm{Im}(k_{\mathrm{mod}})^2]/(v\lvert k_{\mathrm{mod}}\rvert^4) = -\lambda^*_{\mathrm{diff}} h^2/v$
Neutral stability with second-order CT time discretization	
Wave eq.	$\mathrm{Im}(k_{\mathrm{mod}}) = 0$ and $\Delta t \leqslant \min_k 2/(u\lvert k_{\mathrm{mod}}\rvert)$
Convection eq.	$\mathrm{Im}(k_{\mathrm{mod}}) = 0$ and $\Delta t \leqslant \min_k 1/(u\lvert k_{\mathrm{mod}}\rvert)$
Diffusion eq.	$\lvert\mathrm{Re}(k_{\mathrm{mod}})\rvert = \lvert\mathrm{Im}(k_{\mathrm{mod}})\rvert$ and $\Delta t \leqslant \min_k 1/(v\lvert k_{\mathrm{mod}}\rvert^2)$
Exponential stability with first-order BT time discretization	
Wave eq.	$\max_k 2\lvert\mathrm{Im}(k_{\mathrm{mod}})\rvert/(u\lvert k_{\mathrm{mod}}\rvert^2) = \lambda^*_{\mathrm{wave}} h/u < \Delta t$
Convection eq.	$\max_k 2\mathrm{Im}(k_{\mathrm{mod}})/(u\lvert k_{\mathrm{mod}}\rvert^2) = \lambda^*_{\mathrm{conv}} h/u < \Delta t$
Diffusion eq.	$\max_k 2[\mathrm{Im}(k_{\mathrm{mod}})^2 - \mathrm{Re}(k_{\mathrm{mod}})^2]/(v\lvert k_{\mathrm{mod}}\rvert^4) = \lambda^*_{\mathrm{diff}} h^2/v < \Delta t$

occurred over 10^7 random particle distortions. The results reflect the tradeoff between stability and numerical diffusion. Operators that introduce more numerical diffusion (low c) are more robust against Lagrangian grid distortion. We find $c_{\max}$ to be zero for all values of ξ tested if no condition is imposed on the zeroth moment. Of all conditions on the zeroth moment tested, the conditions $Z_h^0 = \{3, 4, 5\}$ result in maximum values for $c_{\max}$.

5.3.2. Discrete time

Discrete-time stability depends on the time discretization scheme. The maximum CFL numbers guaranteeing stable time integration depend on the largest wavenumber-dependent exponents

$$\lambda^*_{\mathrm{conv}} = 2\max_k \frac{\lambda_k^{\mathrm{conv}}}{uh|k_{\mathrm{mod}}|^2}, \quad \lambda^*_{\mathrm{diff}} = 2\max_k \frac{\lambda_k^{\mathrm{diff}}}{vh^2|k_{\mathrm{mod}}|^4}, \quad \lambda^*_{\mathrm{wave}} = 2\max_k \frac{\lambda_k^{\mathrm{wave}}}{uh|k_{\mathrm{mod}}|^2}. \tag{35}$$

Table 4 shows the resulting time-step limits for three cases: (1) first-order forward in time, (2) second-order centered in time, and (3) first-order backward in time.

In case (1) we approximate $\partial f/\partial t$ using first-order FT (forward in time) finite differences (explicit Euler scheme).[2] Von Neumann stability analysis shows that this scheme with time step size Δt is exponentially stable for $|1 + \Delta t b(\hat{\imath} k_{\mathrm{mod}})^\beta| < 1, \ \forall kh \in]0, \pi]$. For the convection equation on symmetric particle distributions, $\lambda_k^{\mathrm{conv}} = 0$ (see Section 5.3.1). Any $\Delta t > 0$ thus leads to instabilities. This is because FTCS (forward in time, central in space) schemes are unstable for hyperbolic partial differential equations. On irregular particle distributions, however, a finite value for $\lambda^*_{\mathrm{conv}}$ is obtained. The more upwind particles are contained in the kernel support, the more likely $\lambda^*_{\mathrm{conv}}$ is negative, leading to exponentially stable explicit Euler time stepping. For the diffusion equation, exponential stability is guaranteed in all cases for $\Delta t < -\lambda^*_{\mathrm{diff}} h^2/v$. Fig. 12 shows the dependence of $\lambda^*_{\mathrm{diff}}$ on the ratio c and the order of accuracy r for uncorrected and DC PSE operators. It can be seen that the underdiffusion introduced for low c and r improves stability. For random particle distributions, a positive upper bound for the time step, i.e. $\lambda^*_{\mathrm{diff}} < 0$, is found for all uncorrected operators and for DC operators with $c < c_{\max}$ (limited Lagrangian grid distortion) and prescribed zeroth-order moment (see Section 5.3.1).

In case (2) we consider the second-order CT (central in time) leapfrog scheme ($a = 1$)

$$f(x, t + \Delta t) = f(x, t - \Delta t) + 2\Delta t Q_h^\beta f(x, t), \tag{36}$$

and the second-order CT scheme ($a = 2$)

$$f(x, t + \Delta t) = 2f(x, t) - f(x, t - \Delta t) + \Delta t^2 Q_h^2 f(x, t). \tag{37}$$

The conditions guaranteeing neutral stability for the one-dimensional wave, convection, and diffusion equations are listed in Table 4. On uniform Cartesian particle distributions neutrally stable solutions of the wave and convection equations can be obtained with all operators. Highly dispersive operators again lead to less restrictive conditions. On random particle distributions, however, none of the tested operators yields stable solutions. For the diffusion equation, none of the operators tested is stable, neither on regular nor on random particle distributions. This is because the first condition in Table 4 is never satisfied for CT schemes.

In case (3) we use first-order BT (backward in time) differences, leading to an implicit time integration scheme. Such schemes have a *lower* bound for the time step required for exponential stability. This limits the accuracy that can be achieved since the time step can not be lowered arbitrarily in order to reduce the approximation error. This is because the BT scheme introduces additional numerical diffusion or dispersion. The neutral stability of the continuous-time case can thus be turned into exponential stability by taking large enough time steps. These lower bounds are listed in Table 4. As expected, they are complementary to the upper bounds of FT schemes: Instead of an upper bound $\Delta t < -\lambda^* h/u$, we now have a lower bound

[2] We do not consider first-order FT schemes for the wave equation since they would involve two unknown values at future time points.

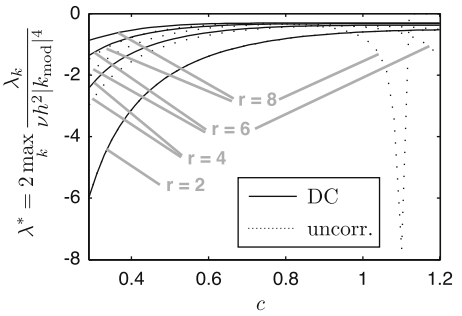

Fig. 12. Influence of the ratio $c = h/\varepsilon$ and the order r on the stability of PSE solutions of the diffusion equation ($\nu > 0$). We show the maxima λ^*_{diff} of the normalized (dimensionless) wavenumber-dependent exponents for uniform Cartesian particle distributions for uncorrected and DC PSE operators.

$\Delta t > \lambda^* h/u$. On uniform Cartesian particle distributions, λ^*_{wave} is zero and exponential stability is guaranteed for all positive time steps. On irregular particle distributions, λ^*_{wave} is positive. From Eqs. (35), (32) and (28) we see that for operators with non-zero Z^1_h, λ^*_{wave} grows as $h^{-1/2}$ when h tends to zero. This implies that the time step Δt can not be decreased at the same rate as the interparticle spacing h. In addition, λ^*_{wave} grows with decreasing c for uncorrected operators. For the convection equation on irregular particle distributions, the lower bound for the time step can be positive or negative, depending on the sign of Z^0_h. As Z^0_h approaches zero, $|\lambda^*_{\text{conv}}|$ grows. Solving the diffusion equation with a BT scheme on uniform Cartesian particle distributions is unconditionally stable ($\lambda^*_{\text{diff}} \leqslant 0$) for all operators. On irregular particle distributions the same is the case for all uncorrected operators and for all DC operators with $c < c_{\max}$ (limited Lagrangian grid distortion) and prescribed zeroth-order moment (see Section 5.3.1).

6. Conclusions

We have presented and analyzed a formal framework for discretization correction of general integral PSE operators [1] for approximating n-dimensional spatial derivatives of any degree. This was made possible by considering the total approximation error, thus combining the mollification and discretization errors. The discrete moments of the kernel function then naturally appeared in the error expansion, and DC operators could be constructed based on the corresponding discrete moment conditions. This also made explicit the connections between DC PSE operators and other space discretization schemes, such as finite differences, corrected SPH, and RKPM. For DC PSE operators, the overlap condition could be relaxed and they became algebraically equivalent to FD stencils in certain limits. We have explicitly shown this equivalence for first derivatives, the Laplacian, and the general n-dimensional anisotropic inhomogeneous diffusion operator.

We have analyzed DC PSE operators with respect to their accuracy, computational efficiency, rate of convergence, and stability on regular and irregular particle distributions as well as near boundaries. We have demonstrated that DC PSE operators achieve the desired rate of convergence in all cases, whereas the convergence of uncorrected operators is hampered by the constant discretization error. The computational efficiency is mainly determined by the cutoff radius of the operators and the ratio c. DC PSE operators are more efficient than uncorrected ones since they reach the same level of accuracy with smaller cutoff radii. Moreover, the relaxed overlap condition of DC PSE operators allows higher values of c, reducing the number of particles within the operator support. For advection-dominated problems, the efficiency of DC PSE operators can exceed that of Lagrangian FD schemes because they require less frequent remeshing and hence are more accurate (less remeshing error). In these cases, the computational cost of determining the position-dependent correction functions is amortized by this gain in accuracy. If remeshing is done at every time step, the remeshing error dominates the error of the diffusion operator and FD schemes are more efficient.

DC operators introduce less numerical diffusion and dispersion into the solution than uncorrected ones. In addition, the numerical diffusion and dispersion of DC PSE operators can be further reduced by increasing c, without affecting the rate of convergence. We have derived analytical expressions for the modified wavenumbers of the one-dimensional wave, convection, and diffusion equations both for uniform Cartesian and random particle distributions. Based on these wavenumbers, we presented CFL-like stability conditions for different time stepping schemes.

The main practical limitation of the presented DC PSE operators lies in determining the DC kernel. We found the approximation error to be sensitive to numerical inaccuracies in the coefficients of the DC kernel. These numerical inaccuracies typically grow with increasing order of convergence, limiting the practical use of high-order operators. Also, the exact conservativeness of uncorrected full-space PSE operators is lost for DC PSE operators on non-uniform particle distributions and near boundaries for $r > 1$. Finally, the computational cost of computing the DC kernel functions on irregular particle distributions is significant, since the correction function has to be determined for each particle individually.

Taken together, our results provide a framework for discretization correction of PSE-type operators. As opposed to the original uncorrected PSE operators, DC operators yield the design rate of convergence over the entire range of resolutions

as well as on irregular particle distributions and near boundaries. Moreover, they offer more freedom in choosing optimal kernel parameters due to the relaxed overlap condition. This can lead to accuracy and efficiency exceeding those of Lagrangian FD schemes.

Acknowledgments

We thank Professor Anthony Leonard for his advice, ideas, and encouraging remarks. B.S. was financed by the Swiss National Science Foundation. S.R. was financed by a grant from the Swiss SystemsX.ch initiative, evaluated by the Swiss National Science Foundation.

Appendix A. Limiting FD stencil of the second-order n-dimensional anisotropic diffusion operator

The anisotropic diffusion operator

$$Df(\boldsymbol{x}) = \nabla\cdot(\boldsymbol{L}(\boldsymbol{x})\nabla f(\boldsymbol{x})) = \sum_{i,j=1}^{n}\frac{\partial}{\partial x_i}\left(L_{ij}(\boldsymbol{x})\frac{\partial f(\boldsymbol{x})}{\partial x_j}\right)$$

can be approximated with second-order accuracy by the PSE operator [8]

$$Qf(\boldsymbol{x}) = \frac{1}{\varepsilon^2}\int_{\mathbb{R}^n}\sum_{i,j=1}^{n}M_{ij}(\boldsymbol{x},\boldsymbol{y})\psi_{ij}^{\varepsilon}(\boldsymbol{y}-\boldsymbol{x})(f(\boldsymbol{y})-f(\boldsymbol{x}))d\boldsymbol{y}. \tag{38}$$

In order for the operator to be symmetric (and hence conservative), the matrix $\boldsymbol{M}(\boldsymbol{x},\boldsymbol{y})$ is chosen as [8]

$$\boldsymbol{M}(\boldsymbol{x},\boldsymbol{y}) = \frac{\boldsymbol{m}(\boldsymbol{x})+\boldsymbol{m}(\boldsymbol{y})}{2},\quad \text{with } \boldsymbol{m}(\boldsymbol{x}) = \boldsymbol{L}-\frac{1}{n+2}\mathrm{Tr}(\boldsymbol{L})\boldsymbol{I}. \tag{39}$$

The continuous moment conditions for the kernel function $\psi_{ij}(\boldsymbol{z})$ are

$$Z_{ij}^{\boldsymbol{\alpha}} = 0 \text{ for } 1\leqslant|\boldsymbol{\alpha}|\leqslant 3 \text{ and } |\alpha|\neq 2, \text{ and}$$
$$\sum_{i,j=1}^{n}m_{ij}(\boldsymbol{x})Z_{ij}^{\boldsymbol{e}_k+\boldsymbol{e}_l} = 2L_{kl}(\boldsymbol{x})\quad \forall k,l\in[1,n],\quad \text{with } Z_{ij}^{\alpha} = \int_{\mathbb{R}^n}\psi_{ij}(\boldsymbol{z})\boldsymbol{z}^{\boldsymbol{\alpha}}\,d\boldsymbol{z}.$$

If the particles are arranged on a uniform Cartesian grid, and using Eq. (39), this translates into the discrete moment conditions

$$Z_{ij}^{\boldsymbol{e}_k+\boldsymbol{e}_l} = 0 \text{ if } i\neq j \quad \text{and } \boldsymbol{e}_k+\boldsymbol{e}_l\neq\boldsymbol{e}_i+\boldsymbol{e}_j, \tag{40a}$$
$$Z_{ij}^{\boldsymbol{e}_i+\boldsymbol{e}_j} = 1 \text{ if } i\neq j, \quad \text{and} \tag{40b}$$
$$Z_{ii}^{2\boldsymbol{e}_i} = 3. \tag{40c}$$

The integral operator Qf (Eq. (38)) is discretized as

$$Q_hf(\boldsymbol{x}) = \frac{1}{\varepsilon^2}\sum_{p}v_p\sum_{i,j=1}^{n}M_{ij}(\boldsymbol{x},\boldsymbol{x}_p)\psi_{ij}^{\varepsilon}(\boldsymbol{x}_p-\boldsymbol{x})(f(\boldsymbol{x}_p)-f(\boldsymbol{x})). \tag{41}$$

DC kernel functions of the form $\psi_{ij}(\boldsymbol{z}) = z_iz_j(a_0+a_1|\boldsymbol{z}|)e^{-\boldsymbol{z}^2},\ i,j=1,\ldots,n$, automatically fulfill condition (40a) and the corresponding operator is given by

$$Q_hf(\boldsymbol{x}) = \frac{c^{n+2}}{2\varepsilon^2}\sum_{|\boldsymbol{k}|^2=0}^{l}\sum_{i,j=1}^{n}(m_{ij}(\boldsymbol{x})+m_{ij}(\boldsymbol{x}+\boldsymbol{k}c\varepsilon))(f(\boldsymbol{x}+\boldsymbol{k}c\varepsilon)-f(\boldsymbol{x}))\times(a_0+a_1c|\boldsymbol{k}|)k_ik_je^{-c^2|\boldsymbol{k}|^2},\quad \boldsymbol{k}\in\mathbb{Z}^n, \tag{42}$$

where $\boldsymbol{k}$ is a vector of integers and $l=\lfloor r_c/h\rfloor^2$ is arbitrary, but large enough to contain the resulting FD stencil. The coefficients a_0 and a_1 are obtained by solving the system of equations that results from substituting the kernel into conditions (40b) and (40c), thus:

$$c^{n+4}\sum_{|\boldsymbol{k}|^2=0}^{l}(a_0+a_1c|\boldsymbol{k}|)k_p^2k_q^2e^{-c^2|\boldsymbol{k}|^2} = 1,\quad p\neq q,$$
$$c^{n+4}\sum_{|\boldsymbol{k}|^2=0}^{l}(a_0+a_1c|\boldsymbol{k}|)k_p^4e^{-c^2|\boldsymbol{k}|^2} = 3.$$

This system can be solved analytically and the coefficients a_0 and a_1 are found as

$$a_0 = \frac{3B - D}{c^{n+4}(BC - AD)}, \quad a_1 = \frac{C - 3A}{c^{n+5}(BC - AD)}, \quad \text{where} \tag{43}$$

$$A = \sum_{|\boldsymbol{k}|^2=0}^{l} k_p^2 k_q^2 e^{-c^2|\boldsymbol{k}|^2}, \quad B = \sum_{|\boldsymbol{k}|^2=0}^{l} |\boldsymbol{k}| k_p^2 k_q^2 e^{-c^2|\boldsymbol{k}|^2}, \quad p \neq q,$$

$$C = \sum_{|\boldsymbol{k}|^2=0}^{l} k_p^4 e^{-c^2|\boldsymbol{k}|^2}, \quad D = \sum_{|\boldsymbol{k}|^2=0}^{l} |\boldsymbol{k}| k_p^4 e^{-c^2|\boldsymbol{k}|^2}.$$

Substituting these coefficients into Eq. (42) yields

$$Q_h f(\boldsymbol{x}) = \frac{1}{2h^2 U} \sum_{|\boldsymbol{k}|^2=0}^{l} \sum_{i,j=1}^{n} (m_{ij}(\boldsymbol{x}) + m_{ij}(\boldsymbol{x} + \boldsymbol{k}c\varepsilon))(f(\boldsymbol{x} + \boldsymbol{k}c\varepsilon) - f(\boldsymbol{x}))(V + W|\boldsymbol{k}|) \times k_i k_j e^{-c^2|\boldsymbol{k}|^2} \quad \text{where}$$

$$U = BC - AD, \quad V = 3B - D, \quad W = C - 3A,$$

which can be rewritten as

$$\begin{aligned} Q_h f(\boldsymbol{x}) = {} & \frac{1}{2h^2 U'''} \sum_{|\boldsymbol{k}|^2=1} \sum_{i,j=1}^{n} (m_{ij}(\boldsymbol{x}) + m_{ij}(\boldsymbol{x} + \boldsymbol{k}c\varepsilon))(f(\boldsymbol{x} + \boldsymbol{k}c\varepsilon) - f(\boldsymbol{x}))(V'' + W'') \times k_i k_j e^{-c^2(|\boldsymbol{k}|^2 - 1)} \\ & + \frac{1}{2h^2 U'''} \sum_{|\boldsymbol{k}|^2=2} \sum_{i,j=1}^{n} (m_{ij}(\boldsymbol{x}) + m_{ij}(\boldsymbol{x} + \boldsymbol{k}c\varepsilon))(f(\boldsymbol{x} + \boldsymbol{k}c\varepsilon) - f(\boldsymbol{x}))\left(V' + \sqrt{2}W'\right) \times k_i k_j e^{-c^2(|\boldsymbol{k}|^2 - 2)} \\ & + \frac{1}{2h^2 U'''} \sum_{|\boldsymbol{k}|^2=3}^{l} \sum_{i,j=1}^{n} (m_{ij}(\boldsymbol{x}) + m_{ij}(\boldsymbol{x} + \boldsymbol{k}c\varepsilon))(f(\boldsymbol{x} + \boldsymbol{k}c\varepsilon) - f(\boldsymbol{x}))(V' + W'|\boldsymbol{k}|) \times k_i k_j e^{-c^2(|\boldsymbol{k}|^2 - 2)}, \end{aligned}$$

where $U''' = Ue^{3c^2}$, $V' = Ve^{c^2}$, $W' = We^{c^2}$, $V'' = Ve^{2c^2}$, $W'' = We^{2c^2}$.

In the limit $c \to \infty$,

$$\lim_{c\to\infty} U''' = 8\left(\sqrt{2} - 1\right), \quad \lim_{c\to\infty} V' = -2, \quad \lim_{c\to\infty} W' = 2, \text{ and } \lim_{c\to\infty}(V'' + W'') = 4\left(\sqrt{2} - 1\right)(4 - n).$$

Hence, we find the operator

$$\begin{aligned} \lim_{c\to\infty} Q_h f(\boldsymbol{x}) = {} & \frac{4 - n}{4h^2} \sum_{|\boldsymbol{k}|^2=1} \sum_{i,j=1}^{n} (m_{ij}(\boldsymbol{x}) + m_{ij}(\boldsymbol{x} + \boldsymbol{k}c\varepsilon))(f(\boldsymbol{x} + \boldsymbol{k}c\varepsilon) - f(\boldsymbol{x}))k_i k_j \\ & + \frac{1}{8h^2} \sum_{|\boldsymbol{k}|^2=2} \sum_{i,j=1}^{n} (m_{ij}(\boldsymbol{x}) + m_{ij}(\boldsymbol{x} + \boldsymbol{k}c\varepsilon))(f(\boldsymbol{x} + \boldsymbol{k}c\varepsilon) - f(\boldsymbol{x}))k_i k_j. \end{aligned} \tag{44}$$

Using the vectors $\boldsymbol{h}_i = h\boldsymbol{e}_i$, $i = 1, \ldots, n$, where $\boldsymbol{e}_i$ is the unit vector along dimension i, this operator can be rewritten as

$$\begin{aligned} \lim_{c\to\infty} Q_h f(\boldsymbol{x}) = {} & \frac{4 - n}{4h^2} \sum_{i=1}^{n} \{(m_{ii}(\boldsymbol{x}) + m_{ii}(\boldsymbol{x} + \boldsymbol{h}_i))(f(\boldsymbol{x} + \boldsymbol{h}_i) - f(\boldsymbol{x})) + (m_{ii}(\boldsymbol{x}) + m_{ii}(\boldsymbol{x} - \boldsymbol{h}_i))(f(\boldsymbol{x} - \boldsymbol{h}_i) - f(\boldsymbol{x}))\} \\ & + \frac{1}{8h^2} \sum_{\substack{i,k=1 \\ i\neq k}}^{n} \{(m_{ii}(\boldsymbol{x}) + m_{ii}(\boldsymbol{x} + \boldsymbol{h}_i + \boldsymbol{h}_k))(f(\boldsymbol{x} + \boldsymbol{h}_i + \boldsymbol{h}_k) - f(\boldsymbol{x})) + (m_{ii}(\boldsymbol{x}) + m_{ii}(\boldsymbol{x} + \boldsymbol{h}_i - \boldsymbol{h}_k))(f(\boldsymbol{x} + \boldsymbol{h}_i - \boldsymbol{h}_k) - f(\boldsymbol{x})) \\ & + (m_{ii}(\boldsymbol{x}) + m_{ii}(\boldsymbol{x} - \boldsymbol{h}_i + \boldsymbol{h}_k))(f(\boldsymbol{x} - \boldsymbol{h}_i + \boldsymbol{h}_k) - f(\boldsymbol{x})) + (m_{ii}(\boldsymbol{x}) + m_{ii}(\boldsymbol{x} - \boldsymbol{h}_i - \boldsymbol{h}_k))(f(\boldsymbol{x} - \boldsymbol{h}_i - \boldsymbol{h}_k) - f(\boldsymbol{x}))\} \\ & + \frac{1}{8h^2} \sum_{\substack{i,j=1 \\ i\neq j}}^{n} \{(m_{ij}(\boldsymbol{x}) + m_{ij}(\boldsymbol{x} + \boldsymbol{h}_i + \boldsymbol{h}_j))(f(\boldsymbol{x} + \boldsymbol{h}_i + \boldsymbol{h}_j) - f(\boldsymbol{x})) - (m_{ij}(\boldsymbol{x}) + m_{ij}(\boldsymbol{x} + \boldsymbol{h}_i - \boldsymbol{h}_j))(f(\boldsymbol{x} + \boldsymbol{h}_i - \boldsymbol{h}_j) - f(\boldsymbol{x})) \\ & - (m_{ij}(\boldsymbol{x}) + m_{ij}(\boldsymbol{x} - \boldsymbol{h}_i + \boldsymbol{h}_j))(f(\boldsymbol{x} - \boldsymbol{h}_i + \boldsymbol{h}_j) - f(\boldsymbol{x})) + (m_{ij}(\boldsymbol{x}) + m_{ij}(\boldsymbol{x} - \boldsymbol{h}_i - \boldsymbol{h}_j))(f(\boldsymbol{x} - \boldsymbol{h}_i - \boldsymbol{h}_j) - f(\boldsymbol{x}))\} \\ = {} & \frac{4 - n}{2} \sum_{i=1}^{n} \left[m_{ii}(\boldsymbol{x}) \frac{\partial^2 f}{\partial x_i^2} + \frac{\partial m_{ii}}{\partial x_i} \cdot \frac{\partial f}{\partial x_i} \right] + \frac{1}{2} \sum_{\substack{i,k=1 \\ i\neq k}}^{n} \left[m_{ii}(\boldsymbol{x}) \left(\frac{\partial^2 f}{\partial x_i^2} + \frac{\partial^2 f}{\partial x_k^2} \right) + \frac{\partial m_{ii}}{\partial x_i} \cdot \frac{\partial f}{\partial x_i} + \frac{\partial m_{ii}}{\partial x_k} \cdot \frac{\partial f}{\partial x_k} \right] \\ & + \sum_{\substack{i,j=1 \\ i\neq j}}^{n} \left[m_{ij}(\boldsymbol{x}) \frac{\partial^2 f}{\partial x_i x_j} + \frac{1}{2} \frac{\partial m_{ij}}{\partial x_i} \frac{\partial f}{\partial x_j} + \frac{1}{2} \frac{\partial m_{ij}}{\partial x_j} \frac{\partial f}{\partial x_i} \right] + \mathcal{O}(h^2) \\ = {} & \sum_{i,j=1}^{n} \frac{\partial}{\partial x_i} \left[L_{ij}(\boldsymbol{x}) \frac{\partial f}{\partial x_j} \right] + \mathcal{O}(h^2) = Df(\boldsymbol{x}) + \mathcal{O}(h^2). \end{aligned}$$

Expressing this in terms of the matrix $\boldsymbol{L}$, instead of the matrix $\boldsymbol{m}$, we find the compact second-order FD stencil for anisotropic diffusion

$$\begin{aligned}
\lim_{c\to\infty} Q_h f(\boldsymbol{x}) = {} & \frac{4-n}{4h^2}\sum_{i=1}^{n}\{(L_{ii}(\boldsymbol{x})+L_{ii}(\boldsymbol{x}+\boldsymbol{h}_i))(f(\boldsymbol{x}+\boldsymbol{h}_i)-f(\boldsymbol{x}))+(L_{ii}(\boldsymbol{x})+L_{ii}(\boldsymbol{x}-\boldsymbol{h}_i))(f(\boldsymbol{x}-\boldsymbol{h}_i)-f(\boldsymbol{x}))\\
& -\frac{1}{n+2}\sum_{k=1}^{n}[(L_{kk}(\boldsymbol{x})+L_{kk}(\boldsymbol{x}+\boldsymbol{h}_i))(f(\boldsymbol{x}+\boldsymbol{h}_i)-f(\boldsymbol{x}))+(L_{kk}(\boldsymbol{x})+L_{kk}(\boldsymbol{x}-\boldsymbol{h}_i))(f(\boldsymbol{x}-\boldsymbol{h}_i)-f(\boldsymbol{x}))]\}\\
& +\frac{1}{8h^2}\sum_{\substack{i,j=1\\ i\neq j}}^{n}\{(L_{ii}(\boldsymbol{x})+L_{ii}(\boldsymbol{x}+\boldsymbol{h}_i+\boldsymbol{h}_j))(f(\boldsymbol{x}+\boldsymbol{h}_i+\boldsymbol{h}_j)-f(\boldsymbol{x}))+(L_{ii}(\boldsymbol{x})+L_{ii}(\boldsymbol{x}+\boldsymbol{h}_i-\boldsymbol{h}_j))(f(\boldsymbol{x}+\boldsymbol{h}_i-\boldsymbol{h}_j)-f(\boldsymbol{x}))\\
& +(L_{ii}(\boldsymbol{x})+L_{ii}(\boldsymbol{x}-\boldsymbol{h}_i+\boldsymbol{h}_j))(f(\boldsymbol{x}-\boldsymbol{h}_i+\boldsymbol{h}_j)-f(\boldsymbol{x}))+(L_{ii}(\boldsymbol{x})+L_{ii}(\boldsymbol{x}-\boldsymbol{h}_i-\boldsymbol{h}_j))(f(\boldsymbol{x}-\boldsymbol{h}_i-\boldsymbol{h}_j)-f(\boldsymbol{x}))+(L_{ij}(\boldsymbol{x})\\
& +L_{ij}(\boldsymbol{x}+\boldsymbol{h}_i+\boldsymbol{h}_j))(f(\boldsymbol{x}+\boldsymbol{h}_i+\boldsymbol{h}_j)-f(\boldsymbol{x}))-(L_{ij}(\boldsymbol{x})+L_{ij}(\boldsymbol{x}+\boldsymbol{h}_i-\boldsymbol{h}_j))(f(\boldsymbol{x}+\boldsymbol{h}_i-\boldsymbol{h}_j)-f(\boldsymbol{x}))-(L_{ij}(\boldsymbol{x})\\
& +L_{ij}(\boldsymbol{x}-\boldsymbol{h}_i+\boldsymbol{h}_j))(f(\boldsymbol{x}-\boldsymbol{h}_i+\boldsymbol{h}_j)-f(\boldsymbol{x}))+(L_{ij}(\boldsymbol{x})+L_{ij}(\boldsymbol{x}-\boldsymbol{h}_i-\boldsymbol{h}_j))(f(\boldsymbol{x}-\boldsymbol{h}_i-\boldsymbol{h}_j)-f(\boldsymbol{x}))\\
& -\frac{1}{n+2}\sum_{k=1}^{n}[(L_{kk}(\boldsymbol{x})+L_{kk}(\boldsymbol{x}+\boldsymbol{h}_i+\boldsymbol{h}_j))(f(\boldsymbol{x}+\boldsymbol{h}_i+\boldsymbol{h}_j)-f(\boldsymbol{x}))+(L_{kk}(\boldsymbol{x})+L_{kk}(\boldsymbol{x}+\boldsymbol{h}_i-\boldsymbol{h}_j))(f(\boldsymbol{x}+\boldsymbol{h}_i-\boldsymbol{h}_j)-f(\boldsymbol{x}))\\
& +(L_{kk}(\boldsymbol{x})+L_{kk}(\boldsymbol{x}-\boldsymbol{h}_i+\boldsymbol{h}_j))(f(\boldsymbol{x}-\boldsymbol{h}_i+\boldsymbol{h}_j)-f(\boldsymbol{x}))+(L_{kk}(\boldsymbol{x})+L_{kk}(\boldsymbol{x}-\boldsymbol{h}_i-\boldsymbol{h}_j))(f(\boldsymbol{x}-\boldsymbol{h}_i-\boldsymbol{h}_j)-f(\boldsymbol{x}))]\}.
\end{aligned}$$

Appendix B. A Two-dimensional advection–diffusion test case

We describe the two-dimensional advection–diffusion problem that is used as a test case in Section 4.4 and provide details on the numerical methods used.

B.1. Testcase description

We solve the dimensionless advection–diffusion equation

$$\frac{\partial f(\boldsymbol{x},t)}{\partial t}+\nabla\cdot(f(\boldsymbol{x},t)\boldsymbol{u}(\boldsymbol{x}))=\frac{\Delta f(\boldsymbol{x},t)}{\mathrm{Pe}},\quad \boldsymbol{x}\in\Omega,\ t\in[0,T]$$

for the unknown field $f(\boldsymbol{x})=f(x,y)$ in the unit square $\Omega=[0,1]^2$. The Péclet number Pe represents the ratio between advection and diffusion. Higher Péclet numbers thus characterize more advection-dominated problems. The advection velocity field $\boldsymbol{u}(\boldsymbol{x})=(y,0)$ is that of a shear flow between two parallel walls. The wall at $y=0$ is fixed whereas the one at $y=1$ moves with unit speed. Both walls are subject to homogeneous Neumann boundary conditions, and we assume periodicity along x. The initial condition is given as

$$f_0(\boldsymbol{x})=f(\boldsymbol{x},t=0)\ =\ \sum_{k=0}^{3}(-1)^k\frac{\cos(2(2k+1)\pi x)}{2k+1},$$

which defines a smooth (regularized) approximation to a rectangular pulse. We consider four different Péclet numbers: $\mathrm{Pe}\in\{1,10,100,1000\}$.

B.2. Reference solution

We compare the numerical results obtained with uncorrected and DC PSE operators to a reference solution at final time

$$T=\frac{\mathrm{Pe}+2-2\sqrt{\mathrm{Pe}+1}}{\mathrm{Pe}}.$$

This is the time at which the mass diffusion length $\sqrt{4T/\mathrm{Pe}}$, added to the maximum distance traveled by a particle due to advection, becomes one. The reference solution is computed using a Lagrangian finite difference method (see Section B.3.3) on a high-resolution grid of 1000×1000 nodes for Pe = {1, 10, 100} and 1600×1600 for Pe = 1000. The L_∞ norm of the relative error – normalized by the concentration range $(\max_{i,j}f_{i,j}^{T/\Delta t}-\min_{i,j}f_{i,j}^{T/\Delta t})$ of the reference solution – is computed after interpolating the reference solution from the grid to the particle locations.

B.3. Method details

We implemented the numerical methods described in the following in Fortran, compiled with the Intel Fortran Compiler v11 with optimization flag `-O3`, and run the simulations on Intel Xeon QuadCore 2.8 GHz processors with 2 GB RAM per core (four simulations per processor, no multithreading). The linear systems of equations of the discretization correction are solved by LU factorization provided by LAPACK [36].

B.3.1. PSE operators

All simulations start with a Cartesian particle distribution of resolution h and use explicit Euler time stepping with $\Delta t \lesssim 0.15h^2\mathrm{Pe}$. Since the advection velocity field is divergence free, the particles have equal and constant volumes $v = h^2$. Their strengths are initialized to $F_p(t=0) = vf_0(\boldsymbol{x}_p(t=0))$. The time evolution of the particle positions and strengths is then given by:

$$\boldsymbol{x}_p(t+\Delta t) = \boldsymbol{x}_p(t) + \Delta t\, \boldsymbol{u}(\boldsymbol{x}_p(t)),$$
$$F_p(t+\Delta t) = F_p(t) + \frac{\Delta t}{\mathrm{Pe}}\left[Q_h^{(2,0)} + Q_h^{(0,2)}\right]F_p(t),$$

where the subscript $p = 1,\ldots,N$ is the particle index. The operators Q_h^{β} are chosen as either DC or uncorrected PSE operators of varying c and r_c (see Section 4.4). The discretization correction is recomputed at each time step unless the particles are remeshed. For irregular particle distributions, the zeroth-order moment of the DC kernels is fixed to $Z_h^{\mathbf{0}} = 5$. The homogeneous Neumann boundary conditions are imposed using mirror particles in a small band outside the domain (method of images).

Remeshing is done by interpolating the particle strengths to a new set of particles with uniform Cartesian positions $\boldsymbol{x}_p$ as:

$$F(\boldsymbol{x}_p) = \sum_{q=1}^{N} \tilde{F}(\tilde{\boldsymbol{x}}_q) W\left(\frac{x_p - \tilde{x}_q}{h}\right) W\left(\frac{y_p - \tilde{y}_q}{h}\right), \tag{45}$$

where W is the third-order accurate M_4' interpolation kernel [37]

$$W(z) = \begin{cases} 0, & |z| > 2, \\ \frac{1}{2}(2-|z|)^2(1-|z|), & 1 \leqslant |z| \leqslant 2, \\ 1 - \frac{5}{2}z^2 + \frac{3}{2}|z|^3, & |z| \leqslant 1. \end{cases}$$

B.3.2. Eulerian finite differences

The solution $f(\boldsymbol{x},t)$ is approximated on a uniform Cartesian grid of resolution h. The values $f_{i,j}^n$ at all grid nodes $\{i,j\}$ are evolved in time $(t = n\Delta t)$ as

$$f_{i,j}^{n+1} = f_{i,j}^n + \frac{\Delta t}{h^2}\left[\frac{1}{\mathrm{Pe}_j'}\left(f_{i+1,j}^n - 2f_{i,j}^n + f_{i-1,j}^n\right) + \frac{1}{\mathrm{Pe}}\left(f_{i,j+1}^n - 2f_{i,j}^n + f_{i,j-1}^n\right) - y_j h(f_{i,j}^n - f_{i-1,j}^n)\right],$$

where $\mathrm{Pe}_j' = 2\mathrm{Pe}/(2 - y_j h\mathrm{Pe})$ if $\mathrm{Pe} \leqslant 2/h$, and $\mathrm{Pe}_j' = \infty$ else. We use a time step of $\Delta t \lesssim \min[0.15h^2\mathrm{Pe}, 0.30h]$. The scheme is second-order accurate for $\mathrm{Pe} \leqslant 2/h$ and first-order otherwise. The Neumann boundary conditions are again imposed using the method of images.

B.3.3. Lagrangian finite differences

The solution is approximated on a uniform Cartesian grid, but advection and diffusion are treated using a time-splitting scheme. In each time step, the grid nodes are advected with the flow and remeshed using the M_4' kernel. Afterward, diffusion is computed using the FD scheme

$$f_{i,j}^{n+1} = f_{i,j}^n + \frac{\Delta t}{h^2\mathrm{Pe}}\left[f_{i+1,j}^n + f_{i-1,j}^n + f_{i,j+1}^n + f_{i,j-1}^n - 4f_{i,j}^n\right]$$

with a time step of $\Delta t \lesssim 0.15h^2\mathrm{Pe}$. The method of images is applied at the Neumann boundaries, and the periodicity is used along x.

Appendix C. Demonstration of the dispersive wavenumber modification in a two-dimensional Eulerian advection test case

We demonstrate the numerical dispersion induced by the wavenumber modification of the operators by simulating advection of a two-dimensional Gauss pulse (Eq. (24)) in direction $\boldsymbol{d} = (0.588, 0.809)$ with unit speed, thus,

$$\frac{\partial f}{\partial t} + \boldsymbol{d}\cdot\nabla f = 0.$$

We approximate $\boldsymbol{d}\cdot\nabla f$ using both uncorrected and DC PSE operators, as well as classical FD stencils. For the DC operators we use the kernel function template in Eq. (8).

Figs. 13 and 14 show the simulation results for second-order $(r=2)$ and fourth-order $(r=4)$ operators, respectively, on uniform Cartesian particle distributions $(h = 0.02)$. The panels show the pulse at times $t = 0$ and $t = 0.5$ in the domain $[-0.1, 1]^2$ with homogeneous Dirichlet boundary conditions. Time integration is done using the leapfrog scheme (Eq. (36)) with a time step of $\Delta t = 0.5h$ for the simulations of order $r = 2$, and $\Delta t = 20h^2$ for the simulations of order $r = 4$.

The results visually illustrate that the order of accuracy r and the ratio c both influence the dispersive properties of the operators. Dispersion decreases with increasing r and c. Since DC PSE operators allow larger values of c at full rate of

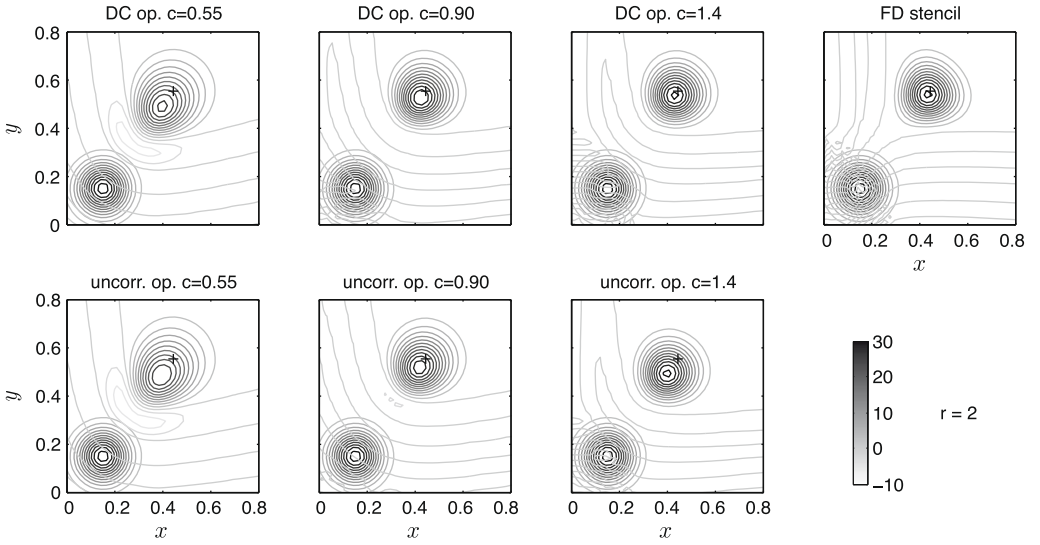

Fig. 13. Effect of numerical dispersion for second-order operators. The contour lines of an advected Gauss pulse (Eq. (24)) are shown at times $t = 0$ and $t = 0.5$. At $t = 0$, the pulse is centered at $\boldsymbol{x} = (0.15, 0.15)$. For $t > 0$, it is propagated along the direction $\boldsymbol{d} = (0.588, 0.809)$ at unit speed. The + marks the center of the pulse in the exact solution at time $t = 0.5$.

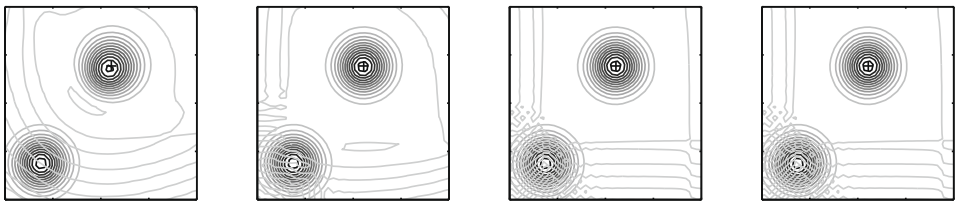

convergence, their numerical dispersion can be reduced down to the level of the FD stencils. This is not possible for uncorrected operators, where the solution gradually deteriorates for increasing c. For low c, PSE operators introduce distortion along direction $\boldsymbol{d}$, whereas the distortion introduced by FD is oriented along the coordinate axes. This is particularly evident for $r = 2$.

References

[1] J.D. Eldredge, A. Leonard, T. Colonius, A general deterministic treatment of derivatives in particle methods, J. Comput. Phys. 180 (2002) 686–709.
[2] P. Degond, S. Mas-Gallic, The weighted particle method for convection–diffusion equations. Part 1: the case of an isotropic viscosity, Math. Comput. 53 (188) (1989) 485–507.
[3] P.A. Raviart, An analysis of particle methods, in: F. Brezzi (Ed.), Numerical Methods in Fluid Dynamics, Lecture Notes in Mathematics, vol. 1127, Springer, Verlag, 1985, pp. 244–323.

[4] R. Cortez, Convergence of high-order deterministic particle methods for the convection–diffusion equation, Commun. Pure Appl. Math. L (1997) 1235–1260.
[5] G.H. Cottet, A particle-grid superposition method for the Navier–Stokes equations, J. Comput. Phys. 89 (1990) 301–318.
[6] S.E. Hieber, P. Koumoutsakos, A Lagrangian particle level set method, J. Comput. Phys. 210 (2005) 342–367.
[7] M. Bergdorf, G.-H. Cottet, P. Koumoutsakos, Multilevel adaptive particle methods for convection–diffusion equations, Multiscale Model. Simul. 4 (1) (2005) 328–357.
[8] P. Degond, S. Mas-Gallic, The weighted particle method for convection–diffusion equations. Part 2: the anisotropic case, Math. Comput. 53 (188) (1989) 509–525.
[9] I.F. Sbalzarini, A. Mezzacasa, A. Helenius, P. Koumoutsakos, Effects of organelle shape on fluorescence recovery after photobleaching, Biophys. J. 89 (3) (2005) 1482–1492.
[10] P. Poncet, Finite difference stencils based on particle strength schemes for improvement of vortex methods, J. Turbul. 7 (23) (2006) 1–24.
[11] C. Golia, B. Buonomo, A. Viviani, A corrected vortex blob method for 3D thermal buoyant flows, Energ. Convers. Manage. 49 (2008) 3243–3252.
[12] P. Koumoutsakos, Inviscid axisymmetrization of an elliptical vortex, J. Comput. Phys. 138 (1997) 821–857.
[13] D. Wee, A.F. Ghoniem, Modified interpolation kernels for treating diffusion and remeshing in vortex methods, J. Comput. Phys. 213 (2006) 239–263.
[14] G.R. Johnson, S.R. Beissel, Normalized smoothing functions for SPH impact computations, Int. J. Numer. Meth. Eng. 39 (1996) 2725–2741.
[15] P.W. Randles, L.D. Libersky, Smoothed particle hydrodynamics: some recent improvements and applications, Comput. Meth. Appl. Mech. Eng. 139 (1996) 375–408.
[16] J. Bonet, S. Kulasegaram, Correction and stabilization of smooth particle hydrodynamics methods with applications in metal forming simulations, Int. J. Numer. Meth. Eng. 47 (2000) 1189–1214.
[17] G. Oger, M. Doring, B. Alessandrini, P. Ferrant, An improved SPH method: towards higher order convergence, J. Comput. Phys. 225 (2007) 1472–1492.
[18] N. Lanson, J.-P. Vila, Convergence des méthodes particulaires renormalisées pour les systèmes de Friedrichs, C.R. Acad. Sci. Paris I 340 (2005) 465–470.
[19] N. Lanson, J.-P. Vila, Renormalized meshfree schemes I: consistency, stability, and hybrid methods for conservation laws, SIAM J. Numer. Anal. 46 (4) (2008) 1912–1934.
[20] N. Lanson, J.-P. Vila, Renormalized meshfree schemes II: convergence for scalar conservation laws, SIAM J. Numer. Anal. 46 (4) (2008) 1935–1964.
[21] W.K. Liu, S. Jun, Y.F. Zhang, Reproducing kernel particle methods, Int. J. Numer. Meth. Fluids 20 (1995) 1081–1106.
[22] W.K. Liu, Y. Chen, R.A. Uras, C.T. Chang, Generalized multiple scale reproducing kernel particle methods, Comput. Meth. Appl. Mech. Eng. 139 (1996) 91–157.
[23] T. Gasser, H.-G. Müller, V. Mammitzsch, Kernels for nonparametric curve estimation, J.R. Stat. Soc. B 47 (2) (1985) 238–252.
[24] V. Mammitzsch, Optimal kernels, Stat. Dec. 25 (2007) 153–172.
[25] G.E. Fasshauer, Meshfree Approximation Methods with MATLAB, World Scientific, 2007.
[26] L. Demkowicz, A. Karafiat, T. Liszka, On some convergence results for FDM with irregular mesh, Comput. Meth. Appl. Mech. Eng. 42 (1984) 343–355.
[27] G.B. Wright, B. Fornberg, Scattered node compact finite difference-type formulas generated from radial basis functions, J. Comput. Phys. 212 (2006) 99–123.
[28] T.-P. Fries, H.-G. Matthies, Classification and overview of meshfree methods, Informatikbericht 2003-03, Technical University Braunschweig (2004).
[29] T. Belytschko, Y. Krongauz, D. Organ, M. Fleming, P. Krysl, Meshless methods: An overview and recent developments, Comput. Meth. Appl. Mech. Engrg. 139 (1996) 3–47.
[30] J.P. Boyd, Chebyshev and Fourier Spectral Methods, second ed., Courier Dover Publications, 2001.
[31] S. Shankar, L. van Dommelen, A new diffusion procedure for vortex methods, J. Comput. Phys. 127 (1996) 88–109.
[32] T.Y. Hou, Convergence of a variable blob vortex method for the Euler and Navier–Stokes equations, SIAM J. Numer. Anal. 27 (6) (1990) 1387–1404.
[33] G.-H. Cottet, P. Koumoutsakos, M.L. Ould Salihi, Vortex methods with spatially varying cores, J. Comput. Phys. 162 (2000) 164–185.
[34] L. Verlet, Computer experiments on classical fluids. I. Thermodynamical properties of Lennard-Jones molecules, Phys. Rev. 159 (1) (1967) 98–103.
[35] F.A. Marvasti, Nonuniform Sampling – Theory and Practice, illustrated ed., Springer, 2001.
[36] E. Anderson, Z. Bai, C. Bischof, S. Blackford, J. Demmel, J. Dongarra, J. Du Croz, A. Greenbaum, S. Hammarling, A. McKenney, D. Sorensen, LAPACK Users' Guide, third ed., Society for Industrial and Applied Mathematics, Philadelphia, PA, 1999.
[37] J.J. Monaghan, Extrapolating B splines for interpolation, J. Comput. Phys. 60 (1985) 253–262.